UC Irvine
UC Irvine Previously Published Works

Title

Toward improved prediction of the bedrock depth underneath hillslopes: Bayesian inference of the bottom-up control hypothesis using high-resolution topographic data

Permalink

https://escholarship.org/uc/item/0qr1q20d

Journal

Water Resources Research, 52(4)

ISSN

Authors

Gomes, Guilherme JC
Vrugt, Jasper A
Vargas, Eurípedes A

Publication Date

2016-04-01

DOI

Peer reviewed

Toward improved prediction of the bedrock depth underneath hillslopes: Bayesian inference of the bottom-up control hypothesis using high-resolution topographic data

Guilherme J. C. Gomes[1,2], Jasper A. Vrugt[2,3], and Eurípedes A. Vargas Jr.[1]

[1]Departamento de Engenharia Civil, Pontifícia Universidade Católica do Rio de Janeiro, Rio de Janeiro, Brazil, [2]Department of Civil and Environmental Engineering, University of California, Irvine, California, USA, [3]Department of Earth System Science, University of California, Irvine, California, USA

Abstract The depth to bedrock controls a myriad of processes by influencing subsurface flow paths, erosion rates, soil moisture, and water uptake by plant roots. As hillslope interiors are very difficult and costly to illuminate and access, the topography of the bedrock surface is largely unknown. This essay is concerned with the prediction of spatial patterns in the depth to bedrock (DTB) using high-resolution topographic data, numerical modeling, and Bayesian analysis. Our DTB model builds on the bottom-up control on fresh-bedrock topography hypothesis of Rempe and Dietrich (2014) and includes a mass movement and bedrock-valley morphology term to extent the usefulness and general applicability of the model. We reconcile the DTB model with field observations using Bayesian analysis with the DREAM algorithm. We investigate explicitly the benefits of using spatially distributed parameter values to account implicitly, and in a relatively simple way, for rock mass heterogeneities that are very difficult, if not impossible, to characterize adequately in the field. We illustrate our method using an artificial data set of bedrock depth observations and then evaluate our DTB model with real-world data collected at the Papagaio river basin in Rio de Janeiro, Brazil. Our results demonstrate that the DTB model predicts accurately the observed bedrock depth data. The posterior mean DTB simulation is shown to be in good agreement with the measured data. The posterior prediction uncertainty of the DTB model can be propagated forward through hydromechanical models to derive probabilistic estimates of factors of safety.

1. Introduction

The depth to bedrock (DTB) controls a large array of geomorphologic, hydrologic, geochemical, ecologic, and atmospheric processes, yet is large unknown as hillslope interiors are very difficult and costly to illuminate and access. The regolith thickness determines groundwater flow [*Freer et al.*, 2002; *Lanni et al.*, 2012], infiltration and redistribution [*Kosugi et al.*, 2006], subsurface saturation [*Tromp-van Meerveld and McDonnell*, 2006b; *Ebel et al.*, 2007; *Liang and Uchida*, 2014], runoff generation [*Troch et al.*, 2002; *Tromp-van Meerveld and McDonnell*, 2006a], storage capacity [*Ohnuki et al.*, 2008], the shape of the hydrograph [*Hopp and McDonnell*, 2009], and variably saturated water flow [*Fujimoto et al.*, 2008]. The bedrock topography is also of paramount importance in geotechnical engineering as it determines slope stability [*Mukhlisin et al.*, 2008; *Ho et al.*, 2012; *Kim et al.*, 2015], pore pressure responses to infiltration [*Vargas Jr. et al.*, 1990; *Askarinejad et al.*, 2012; *Lanni et al.*, 2013], and landslide potential [*Borja and White*, 2010; *Milledge et al.*, 2014; *Bellugi et al.*, 2015]. An accurate characterization of the DTB is thus a prerequisite to describe adequately many different Earth-surface processes.

Spatial patterns in the bedrock depth arise from complex interactions between a myriad of biologic [*Jenny*, 1941], (geo)chemical [*Lebedeva and Brantley*, 2013], and hydrologic [*Rempe and Dietrich*, 2014] processes, and factors including surface topography, lithology [*Catani et al.*, 2010], climate [*Anderson et al.*, 2013], and long-term human activities [*Kuriakose et al.*, 2009]. As a consequence, the thickness of the regolith can vary considerably within a hillslope and watershed, thereby complicating tremendously the characterization and point prediction of the bedrock depth topography [*Catani et al.*, 2010]. Until hillslope interiors are more readily accessible through geophysical imaging or extensive deep drilling, the transition of the underlying fresh bedrock will remain largely unknown [*Rempe and Dietrich*, 2014].

During the past decades, a great deal of research has been devoted to characterization of the soil and regolith depth in headwater hillslopes and catchments. That research has focused primarily on four different issues: (1) the development of specialized measurement techniques for (in)direct observation of the bedrock depth, (2) the application and use of interpolation methods to predict the bedrock depths from sparse direct observations and/or secondary data, (3) the development and application of empirico-statistical methods that predict the spatial continuum of the regolith depth with the help of easily measurable environmental covariates, and (4) the development of landscape evolution models that predict the soil/regolith depth by solving numerically or analytically the soil mass conservation equation.

Research into measurement methods has led to the development and use of direct and indirect sensing techniques to determine the bedrock depth at point and larger support. Examples of direct measurement methods include rod penetrometers [*Kuriakose et al.*, 2009; *Tesfa et al.*, 2009; *Fu et al.*, 2011; *Lanni et al.*, 2012; *Lucà et al.*, 2014], excavated pits [*Boer et al.*, 1996; *Heimsath et al.*, 2001; *Pelletier and Rasmussen*, 2009; *Catani et al.*, 2010; *Pelletier et al.*, 2011], hand and gasoline or electric-powered augers [*Fernandes et al.*, 1994; *Ziadat*, 2010; *Liu et al.*, 2013], road cuts, and erosion gullies [*Kuriakose et al.*, 2009; *Wilford and Thomas*, 2013], and dynamic cone penetrometers [*Kosugi et al.*, 2006, 2009; *Fujimoto et al.*, 2008; *Ohnuki et al.*, 2008; *Tsuchida et al.*, 2011; *Askarinejad et al.*, 2012; *Wiegand et al.*, 2013; *Athapaththu et al.*, 2014; *Liang and Uchida*, 2014]. This last measurement device is particularly promising as it can help delineate soil stratigraphy and layers with contrasting hydraulic properties [*Eguchi et al.*, 2009; *Masaoka et al.*, 2012]. Examples of indirect bedrock depth measurement methods include the use of gravity survey [*Stewart*, 1980; *Bohidar et al.*, 2001], geophysical exploration [*Dahlke et al.*, 2009], seismic refraction [*Zhou and Wu*, 1994], electrical resistivity tomography [*Zhou et al.*, 2000; *Lucà et al.*, 2014], and airborne electromagnetic [*Christensen et al.*, 2015]. These latter five measurement methods make it possible to determine noninvasively the physical properties of the subsurface, yet inversion methods are required to interpret these indirect observations of the bedrock depth. Much effort is required to use these measurement methods to characterize bedrock depth variations at the spatial scale of a hillslope or watershed.

Research into interpolation methods has led to the development and use of (non)linear regression methods to derive regolith depth maps compatible with the application scale of hydrologic and/or geotechnical models. These methods can be classified in two main groups including deterministic and geostatistical interpolation approaches. Deterministic interpolation techniques create a bedrock depth map from measured DTB observations, based on either the extent of similarity between nearby regolith depth observations or the degree of smoothing. Examples include the use of triangulated irregular networks [*Kim et al.*, 2015], inverse distance weighting [*Stewart*, 1980], and radial basis functions, and these approaches work well in the absence of spatial correlation between the measured regolith depth data [*Freer et al.*, 2002; *Wiegand et al.*, 2013]. Geostatistical interpolation techniques capitalize on the spatial structure and semivariance of the measured bedrock depth data [*Goovaerts*, 1997]. Examples include ordinary kriging [*Sitharam et al.*, 2008; *Tye et al.*, 2011], cokriging [*Chung and Rogers*, 2012], and regression-kriging [*Odeh et al.*, 1995; *Sarkar et al.*, 2013]. These methods can incorporate topographic control points derived from digital elevation models and other primary (topographic variables) and secondary (other covariates) variables. Conditional stochastic (Gaussian) simulation can be used to better represent the short-range regolith depth variability derived from geostatistical interpolation [*Kuriakose et al.*, 2009; *Lucà et al.*, 2014]. Interpolation methods are easy to use in practice but require large amounts of field data to derive high-resolution and high-fidelity maps of the bedrock surface topography [*Dietrich et al.*, 1995; *Catani et al.*, 2010; *Liu et al.*, 2013].

Research into empirico-statistical methods has led to the development of multivariate linear/nonlinear or logistic regression methods that predict the bedrock depth from environmental covariates deemed important in soil and regolith formation. These soil-forming factors have been discussed by *Jenny* [1941] in his famous equation and include climate, organisms, relief, parent material, and time. Topographic variables (terrain and landform), bedrock properties (geology and geochemistry), and climatologic characteristics (radiation, precipitation, and temperature) have all been used as predictors of the regolith depth in regression models [*DeRose et al.*, 1991; *Boer et al.*, 1996; *Ziadat*, 2010; *Wilford and Thomas*, 2013; *Yang et al.*, 2014]. Other regression-type methods published in the geomorphologic literature include the use of artificial neural networks [*Zhou and Wu*, 1994; *Mey et al.*, 2015], principal component analysis, and maximum likelihood classification [*Boer et al.*, 1996; *Ziadat*, 2005], canonical correspondence analyses [*Odeh et al.*, 1991], support vector machines [*Sitharam et al.*, 2008], and generalized additive models and random forests [*Tesfa et al.*,

2009; *Shafique et al.*, 2011]. These latter two methods use secondary data of land cover and other soil attributes derived from remote sensing products. Although regression methods have the advantage of being practical and relatively easy to use, the relationship between the regolith depth and exogenous variables (covariates) is empirical and poorly rooted in geomorphologic theory. This complicates their application to out-of-sample prediction in areas outside the domain spanned by the observations.

Research into modeling approaches has led to the development of landscape evolution models that solve the soil mass-balance equation over geological time scales using forward [*Dietrich et al.*, 1995; *Roering*, 2008] or backward simulation [*Pelletier et al.*, 2011]. These geomorphic models simulate processes such as tectonic uplift, regolith production by the underlying bedrock, colluvial transport of the unconsolidated material, erosion, and sedimentation, and have shown to be particularly useful for validation of field observations and hypothesis testing of different soil transport equations. However, the output of landscape evolution models is subject to considerable uncertainty due to errors in the initial states (e.g., topography one or more relief replacement times ago), boundary conditions (climate and tectonic forcing), geologic characterization (e.g., bedrock properties), parameter values, model structure, and equations. If conditions of dynamic equilibrium between soil production and erosion are assumed, then simple closed-form parametric solutions can be derived for the soil thickness by solving analytically the soil conservation equation for certain specific formulations of the soil transport equation and/or soil production function [*Bertoldi et al.*, 2006; *Saco et al.*, 2006; *Pelletier and Rasmussen*, 2009]. These analytic solutions allow for predictive mapping of the soil thickness from high-resolution topographic data and field-based calibration [*Pelletier and Rasmussen*, 2009]. Examples include the nonlinear slope-dependent, nonlinear depth, and slope-dependent, and nonlinear area and slope-dependent transport functions of *Pelletier and Rasmussen* [2009]. These analytic models describe accurately thin soil depth beneath hillslope ridges, but it has yet to be established whether they can predict adequately concave hillslopes with relatively thin soils. This may give preference instead to simulation of instantaneous DTB maps using high-resolution topographic data [*Saulnier et al.*, 1997; *Bertoldi et al.*, 2006; *Catani et al.*, 2010].

In a separate line of research, *Catani et al.* [2010] have proposed an empirical geomorphology-based model to predict the bedrock depth at the catchment scale using relative position, hillslope gradient, and curvature. This model was shown to describe accurately the observed regolith depths of Italian watersheds. *Liu et al.* [2013] have derived a simple analytic expression of the soil mass balance equation for humid and semihumid climates without tectonic activity in the immediate geological past. The simulated soil depths of this model match closely the observed bedrock depths at the 7.9 ha Shale Hills catchment in the United States with root mean square error of 0.39 m and $R^2 = 0.74$. These closed-form analytic models of the regolith thickness are much easier to implement and use in practice than numerical landscape evolution models requiring only a high-resolution topographic map and some calibration against observed regolith depth data to predict the bedrock surface. Recently, *Rempe and Dietrich* [2014] have introduced an alternative analytic model that predicts the hillslope form and the vertical extent of the weathered rock underling soil-mantled hillslopes using physical parameters such as permeability of the intact rock mass, porosity, and the rate of channel incision at the base of the hillslope. This model builds on the assumption that once the fresh bedrock, saturated with nearly stagnant fluid, is advected into the near surface through uplift and erosion, channel incision produces a lateral head gradient within the fresh bedrock inducing drainage toward the channel. The slow drainage of the fresh bedrock exerts an bottom-up control on the advance of the weathering front, suggesting that bedrock discontinuities and fractures can play a major role in regolith production [*Clair et al.*, 2015]. The model of *Rempe and Dietrich* [2014] produces thick weathered zones beneath ridges and thin regolith depths beneath valleys, and has the advantage of being fully testable. Most of the model parameters can be measured directly in the laboratory or field using experiments on soil and rock mass samples, and the simulated variables can be verified using cosmogenic nuclide measurements, geophysical imaging, topographic surveying, and drilling.

Whereas much progress has been made on the development and use of models for prediction of the regolith thickness, surprisingly little attention has been given to inference of their parameters. Many of the parameters in these models cannot be measured directly in the field but can only be meaningfully inferred from field data. What is more, some parameters might be depth-dependent or vary spatially depending on hillslope position and lithology. In this paper, we build on the ideas of *Pelletier and Rasmussen* [2009], *Catani et al.* [2010], and *Rempe and Dietrich* [2014] and introduce a Bayesian framework for DTB model parameter

estimation. The Bayesian paradigm provides a simple way to address systematically different sources of uncertainty within a single cohesive, integrated framework [*Vrugt et al.*, 2008]. We use Markov chain Monte Carlo (MCMC) simulation with the DiffeRential Evolution Adaptive Metropolis (DREAM) algorithm [*Vrugt et al.*, 2008, 2009] to infer the parameters of the DTB model from spatially distributed regolith depth observations. This model builds on the bottom up control of fresh bedrock hypothesis of *Rempe and Dietrich* [2014] and uses a slope-dependency and a bedrock-valley shape term to extent the usefulness and general applicability of the model. The DREAM algorithm has been applied to many different fields of study involving lumped [*He et al.*, 2011; *Scharnagl et al.*, 2011] and spatially distributed, high-dimensional, parameter spaces [*Keating et al.*, 2010; *Laloy et al.*, 2013; *Linde and Vrugt*, 2013; *Lochbühler et al.*, 2014]. We investigate explicitly the benefits of using spatially distributed DTB parameter values for the prediction of bedrock depths. Such parameterization provides a means to account implicitly, and in a relatively simple way, for system heterogeneities that are difficult, or impossible, to characterize adequately in the field. We illustrate our method using synthetic bedrock depth observations and validate our approach with real-world data collected at the Papagaio river basin (PRB) in Rio de Janeiro, Brazil. The PRB watershed has been the subject of much study in the literature [*Guimarães et al.*, 2003; *Fernandes et al.*, 2004; *Vieira and Fernandes*, 2004; *Gomes et al.*, 2008, 2013] but this previous work has focused primarily on unraveling the mechanisms of mass movement rather than modeling of the bedrock depth.

The remainder of this paper is organized as follows. Section 2 reviews the basic building blocks of the DTB model. Then in section 3, we evaluate the sensitivity of each of the DTB model parameters to the simulated bedrock surface for a synthetic hillslope topography. This section will help build awareness and intuition on how the different DTB model parameters affect the simulated bedrock profiles. This is followed in section 4 with a short introduction to Bayesian analysis (inversion) for inference of the DTB model parameters. In this section, we are especially concerned with the description of the DREAM algorithm used to sample the posterior parameter distribution. We then proceed with a discussion of the DTB inversion results for a synthetic (section 5) and real-world (section 6) regolith depth data set using lumped and spatially distributed parameter values. Section 7 of this paper discusses the implications of our results for hydrologic and geotechnical modeling and engineering. Finally, section 8 concludes this paper with a summary of the main findings.

2. Model Description

In this section, we introduce the different building blocks of our DTB model which is used herein to predict the hillslope form and the vertical extent of the weathered rock underling soil-mantled hillslopes from a high-resolution topographic map of the soil surface. We assume herein that regolith thickness depends on the interplay between erosion, which removes unconsolidated material from the ground surface, and weathering, which promotes rock fragmentation in the soil-bedrock interface. Our model builds on the bottom-up control on fresh-bedrock hypothesis of *Rempe and Dietrich* [2014] and calculates the thickness of the weathered zone from the difference between the measured surface topography and predicted groundwater profile derived from analytic solution of the one-dimensional steady state Boussinesq equation [*Bear*, 2013]. Two additional terms are used to characterize adequately the morphology of the bedrock surface beneath the drainage valley, and the regolith thickness on steep slopes subject to an increased sediment flux due to mass movement.

The regolith thickness, h [L] of a soil-mantled hillslope can be derived by calculating the difference between the elevation of the ground surface, Z_s [L] and the underlying topography, Z_b [L] of the fresh bedrock

$$h(x,y) = Z_s(x,y) - Z_b(x,y), \tag{1}$$

where the coordinates (x, y) are used to denote spatial location. Spatial maps of Z_s are readily available from digital elevation models (DEMs), yet the topography of the fresh bedrock, Z_b is largely unknown as the interior of a hillslope is very difficult and costly to access. Relatively few publications can be found in the geomorphologic literature that have documented directly the depth to the fresh bedrock underlying ridge and valley topography [*Ruxton and Berry*, 1959; *Thomas*, 1966]. Those studies that have mapped Z_b have illuminated that the weathered zone is thickest at the ridge top and gets progressively thinner downslope [*Ruxton and Berry*, 1959; *Thomas*, 1966; *Ruddock*, 1967; *Feininger*, 1971]. What is more, detailed studies of weathering profiles published many decades ago have identified that groundwater can impede chemical

weathering thereby restricting the depth of the weathered zone [*Ruxton and Berry*, 1959; *Thomas*, 1966]. These early experimental findings have stimulated *Rempe and Dietrich* [2014] to suggest a new hypothesis for rock mass weathering underlying soil-mantled hillslopes. This hypothesis assumes that the groundwater exerts a bottom-up control on fresh bedrock topography, and explains published experimental findings of progressively thinner weathered zones downslope. This hypothesis is diametrically opposed to the classic top-down hypothesis that is used by many soil depth models. The top-down hypothesis links the soil thickness to processes taking place at the ground surface by assuming that the thickness of the weathered zone is set by the relative rates of erosion and the soil production in the weathering front.

The bedrock depth model of *Rempe and Dietrich* [2014] builds on the one-dimensional, steady state form of the Boussinesq equation for groundwater flow [*Bear*, 2013]

$$\frac{1}{2}K\frac{\partial^2 Z_b^2}{\partial x^2}+\phi C_o=0, \tag{2}$$

where K [LT^{-1}] denotes the saturated hydraulic conductivity of the bedrock, x [L] is the horizontal distance from the ridge, ϕ [-] signifies the saturated drainable pore space of the bedrock (= porosity), and C_o [LT^{-1}] represents the channel incision rate at the base of the hillslope. By assuming strictly horizontal flow, topographic symmetry about the ridge, and a channel elevation at the bottom of the hillslope, the following closed-form equation can be derived for the elevation of the transition from fresh to weathered bedrock

$$Z_b(x)=\sqrt{\frac{\phi C_o}{K}\left(L^2-x^2\right)}, \tag{3}$$

where L [L] is the hillslope length, and the term (L^2-x^2) can be interpreted as distance to the drainage channel. A step-by-step derivation of equation (3) is given in the supporting information of *Rempe and Dietrich* [2014], and thus will not be repeated herein. Equation (3) predicts that the depth of the weathered zone decreases from the hilltop to the valley floor with convexity and depth of the bedrock surface determined by the parameters ϕ, C_o, K.

Our DTB model uses as basic building block the analytic solution of equation (3) but includes two important extensions that enhance applicability of the model to watersheds with convex and/or concave bedrock surfaces underneath the drainage valley and thin weathered zones and/or exposed rock on steep hillslopes subject to mass movement. This DTB model solves for the bedrock depth at two spatial coordinates, x and y and contains two new variables, Ψ and Λ whose values are derived from the slope angle and drainage distance, respectively, and three additional (quasi)-physical parameters. The basic formulation of the DTB model is given by the following closed-form equation

$$Z_b(x,y)=\frac{\Psi}{\Lambda}\sqrt{\Phi L_d^2(x,y)}, \tag{4}$$

where Ψ [-] measures the effect of mass movement on the bedrock surface, Λ [-] determines the shape and depth of the bedrock valley, and is hereafter also referred to as the bedrock-valley shape term, L_d [L] denotes the horizontal distance from the drainage, and $\Phi=\phi C_0/K$ [-] is a scalar that summarizes conveniently the combined effect of rock porosity, permeability, and the channel incision rate on the elevation of the fresh bedrock, Z_b. The scalar variables Λ and Ψ are bounded between zero and one and determine the regolith thickness underneath valleys and steep slopes. The drainage distance, $L_d(x,y)$, of each spatial location in the watershed is derived from the surface topography using recursive DEM computation [*Tesfa et al.*, 2009; *Catani et al.*, 2010]. No distinction has to be made between drainage lines and hillslope lines to predict $Z_b(x,y)$ underneath the watershed. Thus a single call to equation (4) suffices to derive the elevation of the bedrock surface for given (x, y) coordinates.

Mass movement is described in analogy with the nonlinear slope-dependent model of *Roering et al.* [1999]

Table 1. Summary and Description of the Main Variables of the DTB Model

Symbol	Unit	Type	Description
Z_x	[-]	Model input	Slope gradient in x direction
Z_y	[-]	Model input	Slope gradient in y direction
L_d	[L]	Model input	Drainage distance
$\bar{L}_d$	[-]	Model input	Normalized drainage distance
Φ	[-]	Model parameter	Equivalent to $\phi C_o/K$
λ_1	[-]	Model parameter	Bedrock-valley morphology parameter
λ_2	[-]	Model parameter	Bedrock-valley morphology parameter
S_c	[-]	Model parameter	Critical angle of slope stability

$$\Psi = 1 - \min\left[1, \left(|\nabla Z_s|/S_c\right)^2\right], \tag{5}$$

where ∇Z_s [-] denotes the slope gradient of the surface topography and S_c [-] signifies the critical slope angle beyond which mass movement is initiated. We follow *Perron* [2011], and calculate the norm $|\nabla Z_s|$ using

$$|\nabla Z_s| = \sqrt{Z_{s,x}^2 + Z_{s,y}^2}, \tag{6}$$

where $Z_{s,x}$ [-] and $Z_{s,y}$ [-] are the gradients of the slope in the x and y direction, respectively. Equation (5) predicts regolith loss on hillslopes steeper than the threshold angle S_c. This movement of mass (due to landslides) gives rise to exposed rock.

The variable Λ in equation (4) determines the hillslope-to-valley transition morphology and is computed as follows

$$\Lambda = \exp\left[-\lambda_1\left(1 - \bar{L}_d\right)^{\lambda_2}\right], \tag{7}$$

where $\bar{L}_d$ [-] denotes the normalized drainage distance, and λ_1 and λ_2 are dimensionless shape parameters that determine the bedrock shape (curvature) and depth in the valley at the base of the hillslope. This provides a mechanism to better describe the topographic signature of valley incision by debris flow and landslides [*Tarolli and Fontana*, 2009]. Table 1 summarizes the main variables and parameters of the DTB model. The effects of the variables Ψ and Λ on the predicted spatial distribution of the regolith thickness are discussed in the next section.

3. Parameter Sensitivity Analysis

To test the predictive capability of the DTB model, we confront the model with regolith depth data of a typical hillslope of Rio de Janeiro. We first benchmark the model using an artificial topographic surface derived from n_s different sine waves

$$Z_s(x) = \sum_{i=1}^{n_s} \omega_i \sin\left(\beta_i x + \chi_i\right), \tag{8}$$

where x [L] is the horizontal distance along the hillslope, and ω, β, and χ are unitless coefficients that signify the amplitude, frequency, and phase of each individual sine wave. The synthetic surface topography used herein was derived by setting $n_s = 2$ and using values of the coefficients of equation (8) listed in Table 2.

Figure 1 now presents a sensitivity analysis of the parameters of the DTB model. The four different horizontal plots show the DTB model predicted regolith profiles underneath the artificial hillslope for different values of the parameters Φ (top), λ_1 (top-middle), λ_2 (bottom-middle), and S_c (bottom). The artificial topography (surface) of equation (8) is separately indicated in each plot with the black line. The results of Figure 1 will help build intuition and insights on how the different parameters of the DTB model affect the simulated bedrock surface topography. The landscape elements "hilltop," "sideslope," and "drainage" are used herein to discuss our findings. Their position is indicated in Figure 1a.

Before we proceed with the main findings of the sensitivity analysis, we first interpret all the simulated bedrock depth profiles of the DTB model displayed in Figure 1. Regardless of the parameter values used in the DTB model, the weathered zone appears largest at the hilltop and then progressively thins downward. This profile of the bedrock depth underneath the hillslope is in agreement with field observations of upland and lowland areas [*Liang and Uchida*, 2014; *Kim et al.*, 2015] and mimics qualitatively the output of the *Rempe and Dietrich* [2014] model. The effect of the parameter S_c (regolith movement due to landslides) on the output of the DTB model is shown in Figures 1g and 1h and reduces, as expected, the thickness

Table 2. Parameters of the Synthetic Topographic Surface Model

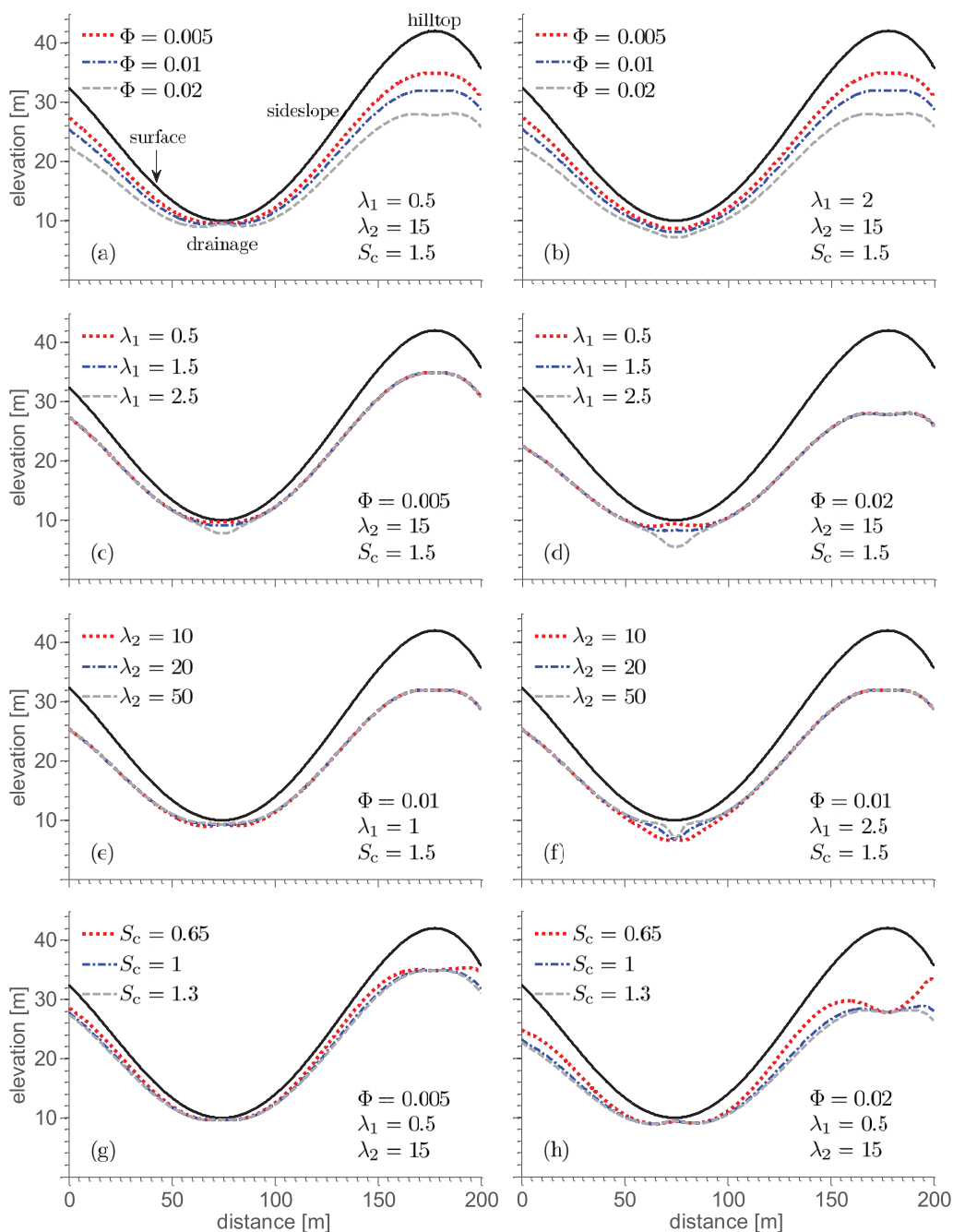| Description	Symbol	Index of sine wave	
		1	2
Amplitude	ω	11,880	11,630
Frequency	β	0.012	0.012
Phase constant	χ	0.661	3.790

Figure 1. Sensitivity of the bedrock depth profile predicted by the DTB model to the values of the parameters Φ (a and b), λ_1 (c and d), λ_2 (e and f), and S_c (g and h). The dotted lines in red, blue, and gray display the simulated bedrock profiles for the listed values of the DTB-model parameters. The surface topography is separately indicated in each plot with the solid black line. The top-left graph (a) clarifies the position of the landscape elements "hilltop," "sideslope," and "drainage" that are used to discuss our findings.

of the weathered zone along the sideslope. The effect of the DTB variable Λ (hillslope-to-valley morphology) is visible in most of the displayed bedrock depth profiles with a shape and curvature of the bedrock surface in the valley (drainage) that deviates considerably from the concave drainage profiles simulated exclusively by equation (3) of *Rempe and Dietrich* [2014].

We now move on to the results of the sensitivity analysis. The top plot in Figure 1a shows that larger values of the parameter Φ increase the thickness of the unweathered zone underneath the hillslope. This increase in bedrock depth is largest at the hilltop (as explained by for instance a high rock permeability), and gets

progressively smaller downslope toward the base of the hillslope (drainage). The morphology of the bedrock surface in the valley appears gently convex, but assumes a concave shape when the value of parameter λ_1 is increased from 0.5 to 2 (see Figure 1b).

The top-middle plot (second from top) of Figure 1 illustrates the effect of λ_1 on the simulated bedrock depth profiles. It is evident that this parameter affects only the bedrock depth topography and curvature in the valley. For $\lambda_1 = 0.5$ in Figures 1c and 1d, the unweathered zone in the valley (drainage) is really thin and the bedrock surface is almost exposed at the center of the channel. As will be shown in the next plot (bottom-middle) this result is independent on the value of λ_2. A convex curvature of the bedrock surface emerges below the channel when Ψ is increased from 0.005 in Figure 1c to 0.02 in Figure 1d. For larger values of λ_1, the thickness of the unweathered zone increases with a smooth bedrock-valley shape for $\lambda_1 = 1.5$ and V-shape bedrock surface for $\lambda_1 = 2.5$.

The bottom-middle plot in Figure 1 displays how parameter λ_2 affects the predicted elevation of the bedrock surface topography. The DTB simulated bedrock depth on the hilltop and sideslope appears insensitive to parameter λ_2. Indeed, values of λ_2 of 10, 20, and 50 give an exactly similar bedrock elevation underneath the sideslope and hilltop. The same holds true for the thickness of the weathered zone exactly at the midpoint of the drainage channel. The elevation of the fresh bedrock at this lowest point of the surface topography is fixed for different values of λ_2. Beyond this center-point, the bedrock depth varies as function of λ_2, the extent to which depends on the value of λ_1. As is evident from Figure 1e, for relatively low values of λ_1 the bedrock topography simulated by the DTB model does not depend on λ_2. However, this sensitivity of the DTB model output to λ_2 increases for larger values of λ_1. Indeed, Figure 1f shows an increasingly V-shaped morphology of the bedrock surface underneath the drainage valley. The results presented herein demonstrate that the shape and depth of the bedrock surface underneath the valley is determined by parameters λ_1 and λ_2 and thus the value of Λ in equation (4) of the DTB model. Recent research indicates that the elevation and curvature of the bedrock surface in the valley might be explained by the horizontal stress field [*Clair et al.*, 2015].

The bottom plot in Figure 1 shows the effect of S_c on the simulated regolith profiles. The effect of mass movement is most noticeable for the bedrock topography underneath the sideslope as the depth of the weathered zone at the hilltop and the drainage valley appear unaffected. The larger the value of the critical slope angle, the more unlikely mass movement will take place, and thus the more similar the DTB model simulated depth to bedrock underneath the slope. Indeed, the bedrock profiles for $S_c = 1$ and $S_c = 1.3$ are in excellent agreement and follow closely the shape of the topographic surface. For smaller values of S_c, however the slope angle simulated by the DTB model approaches a critical threshold of about 27° and the thickness of the weathered zone beneath the hillslope decreases considerably. This is readily visible in Figure 1h (dotted red line). The thickness of the regolith has decreased substantially in the steepest part of the hillslope just below the hilltop, and the weathered zone approaches an approximately fixed depth from the inflection point downwards toward the drainage valley. This trend is in agreement with our field knowledge from hillslopes in Rio de Janeiro, Brazil. We therefore posit that our DTB model can be used for hillslopes with steep gradients whose underlying fresh-bedrock surface is determined by rock properties (low values of Φ in Figure 1g) and surface steeping (Figure 1h). Note that for $S_c = 0.65$ the DTB model predicts a rather peculiar bedrock depth at the sideslope. At this point, it is not clear whether this constitutes a structural limitation (epistemic error) of equation (4) or whether this highlights an issue with the parameter values.

In summary, the parameter Φ (rock properties) determines the depth to bedrock underneath the sideslope and hilltop. The parameter S_c (critical slope angle) can activate the process of mass movement (if set sufficiently small) and this affects the angle of the bedrock surface and depth of the regolith beneath the sideslope. The parameters λ_1 and λ_2 determine the shape (convex/concave) and depth of the bedrock surface in the drainage valley. With these four fitting parameters the DTB model as proposed herein, can simulate the bedrock surface of convergent and divergent hillslopes.

A final remark about the results of the sensitive analysis is appropriate. The bedrock depths shown in Figure 1 suggest that the parameters λ_1 and λ_2, as they appear in equation (7), might be correlated as they both determine the topography of the valley-bedrock surface. We will revisit this issue of parameter identifiability (and lack thereof) in section 5.1 of this paper. We are now left with a treatment of the DTB model parameters. Their values are catchment (hillslope)-dependent and need to be derived by fitting the model against spatially distributed observations of DTB.

4. Inverse Modeling

The DBT model contains several coefficients that are difficult to be measured directly in the field at the application scale of interest, and thus have to be determined by calibration instead using some spatially distributed map of regolith depth observations. If we denote with $\mathcal{F}$ equation (4), then we can write our DTB model as follows

$$\mathbf{H} \leftarrow \mathcal{F}(\theta, \nabla Z_s, \mathbf{L}_d) + \mathbf{e}, \tag{9}$$

where $\mathbf{H} = \{h_1, \ldots, h_n\}$ is a n-vector of simulated bedrock depths at spatial coordinates, $(x_1, y_1) \ldots (x_n, y_n)$, $\theta = \{\Phi, \lambda_1, \lambda_2, S_c\}$ signifies the d-vector of model parameters, $\mathbf{L}_d = \{L_d(x_1, y_1), \ldots, L_d(x_n, y_n)\}$ stores the n-values of the drainage distance of each measurement location, and $\mathbf{e} = \{e_1, \ldots, e_n\}$ represents the vector of observation errors. The vector $\mathbf{e}$ includes observation error as well as error due to the fact that the DTB model, $\mathcal{F}(\cdot)$ may be systematically different from reality, $\Im(\theta)$ for the parameters θ. The latter may arise from an improper model formulation (epistemic errors) and topographic uncertainty (due to DEM measurement errors and/or inadequate resolution).

If we adopt a Bayesian formalism then we can derive the posterior distribution of the parameters, $p(\theta|\tilde{\mathbf{H}})$, by conditioning the spatial behavior of the model on the n-measured values of the bedrock depth, $\tilde{\mathbf{H}} = \{\tilde{h}_1, \ldots, \tilde{h}_n\}$ using

$$p(\theta|\tilde{\mathbf{H}}) = \frac{p(\theta)p(\tilde{\mathbf{H}}|\theta)}{p(\tilde{\mathbf{H}})}, \tag{10}$$

where $p(\theta)$ is the prior parameter distribution, $L(\theta|\tilde{\mathbf{H}}) \equiv p(\tilde{\mathbf{H}}|\theta)$ denotes the likelihood function, and $p(\tilde{\mathbf{H}})$ signifies the evidence. This latter variable is a constant that is independent of the parameter values and acts as a normalization constant (scalar) so that the posterior distribution integrates to unity

$$p(\tilde{\mathbf{H}}) = \int_\Theta p(\theta)p(\tilde{\mathbf{H}}|\theta)\mathrm{d}\theta = \int_\Theta p(\theta, \tilde{\mathbf{H}})\mathrm{d}\theta, \tag{11}$$

over the parameter space, $\theta \in \Theta \in \mathbb{R}^d$. In practice, $p(\tilde{\mathbf{H}})$ is not required for posterior estimation as all statistical inferences about $p(\theta|\tilde{\mathbf{H}})$ can be made from the unnormalized density

$$p(\theta|\tilde{\mathbf{H}}) \propto p(\theta)L(\theta|\tilde{\mathbf{H}}). \tag{12}$$

We conveniently assume that the prior distribution, $p(\theta)$ is uniform, $p(\theta) \propto c$, where c is a constant. This means that we a-priori do not favor any values of the model parameters, and instead use uniform prior ranges. The main culprit now resides in the definition of the likelihood function, $L(\theta|\tilde{\mathbf{H}})$, used to summarize the distance between the model simulations, $\mathbf{H}(\theta)$, and corresponding observations, $\tilde{\mathbf{H}}$. If we assume the error residuals of the observed and simulated bedrock depths to be normally distributed and uncorrelated, then the likelihood function can be written as

$$L(\theta|\tilde{\mathbf{H}}) = \prod_{i=1}^n \frac{1}{\sqrt{2\pi\hat{\sigma}_i^2}} \exp\left[-\frac{1}{2}\left(\frac{\tilde{h}_i - h_i(\theta)}{\hat{\sigma}_i}\right)^2\right], \tag{13}$$

where $\hat{\sigma}_i$ is an estimate of the standard deviation of the measurement error of the ith regolith depth observation. This formulation allows for homoscedastic (constant variance) and heteroscedastic measurement errors (variance dependent on magnitude of each data point). If homoscedasticity is expected and the variance of the error residuals, $s^2 = \frac{1}{n-1}\sum_{t=1}^n (e_t(\theta))^2$ is taken as sufficient statistic for σ^2, then one can show that the likelihood function simplifies to

$$L(\theta|\tilde{\mathbf{H}}) \propto \sum_{i=1}^n |\tilde{h}_i - h_i(\theta)|^{-n}. \tag{14}$$

Once the prior distribution and likelihood function have been defined, what is left in Bayesian analysis is to summarize the posterior distribution. For models such as equation (4) which is nonlinear in its parameters, the posterior distribution $p(\theta|\tilde{\mathbf{H}})$ cannot be obtained by analytic means nor by analytic approximation. We therefore resort to iterative methods that approximate the posterior probability density function by

generating a large sample from this distribution. The most powerful of such sampling methods is Markov chain Monte Carlo (MCMC) simulation using the Metropolis algorithm [*Metropolis et al.*, 1953]. The basis of MCMC simulation is a Markov chain that generates a random walk through the search space and successively visits solutions with stable frequencies stemming from a stationary distribution, $\bar{\pi}(\cdot)$. To explore the target distribution, $\bar{\pi}(\cdot)$, a MCMC algorithm alternates between three basic steps. First, a proposal θ_p is generated from the current state of the Markov chain, θ_t using some jumping distribution, $q(\theta_t \rightarrow \theta_p)$. Next, this proposal is accepted with Metropolis probability

$$P_{acc}(\theta_t \rightarrow \theta_p) = \min \left[1, \frac{p(\theta_p)q(\theta_p \rightarrow \theta_t)}{p(\theta_t)q(\theta_t \rightarrow \theta_p)} \right]. \tag{15}$$

Finally, if the proposal is accepted, the chain moves to θ_p, and thus $\theta_{t+1} = \theta_p$, otherwise the current position is retained, $\theta_{t+1} = \theta_t$. Repeated application of these three steps results in a Markov chain which, under certain regularity conditions, has a unique stationary distribution with posterior probability density function, $\bar{\pi}(\cdot)$. In practice, this means that if one looks at the values of θ sufficiently far from the arbitrary initial value, that is, after a burn-in period, the successively generated states of the chain will be distributed according to $\bar{\pi}(\cdot)$, the d-dimensional posterior probability distribution of θ. Burn-in is required to allow the chain to explore the search space and reach its stationary regime.

If a symmetric jumping distribution is used, that is $q(\theta_t \rightarrow \theta_p) = q(\theta_p \rightarrow \theta_t)$, then equation (15) simplifies to

$$P_{acc}(\theta_t \rightarrow \theta_p) = \min \left[1, \frac{p(\theta_p)}{p(\theta_t)} \right]. \tag{16}$$

This selection rule has become the basic building block of the random walk Metropolis (RWM) algorithm, the earliest MCMC method. This RWM algorithm can be coded in just a few lines and requires only a jumping distribution, a function to generate uniform random numbers, and a function to calculate the probability density of each proposal, which is simply equivalent to the product of the prior distribution and likelihood function of equation (14).

The efficiency of the RWM algorithm is determined by the choice of the proposal distribution, $q(\cdot)$ used to create trial moves (transitions) in the Markov chain. When the proposal distribution is too wide, too many candidate points are rejected, and therefore the chain will not mix efficiently and converge only slowly to the target distribution. On the other hand, when the proposal distribution is too narrow, nearly all candidate points are accepted, but the distance moved is so small that it will take a prohibitively large number of updates before the sampler has converged to the target distribution. The choice of the proposal distribution is therefore crucial and determines the practical applicability of MCMC simulation in many fields of study [*Vrugt*, 2016].

In this paper, MCMC simulation of the DTB model has been performed using the DREAM algorithm [*Vrugt et al.*, 2008, 2009]. This multichain MCMC simulation algorithm automatically tunes the scale and orientation of the proposal distribution, $q(\cdot)$ en route to the target distribution. This is one of the reasons DREAM exhibits excellent sampling efficiencies on complex, high-dimensional, and multimodal target distributions. The use of multiple chains offers a robust protection against premature convergence, and opens up the use of a wide arsenal of statistical measures to test whether convergence to the posterior distribution has been achieved. We evaluate the DTB model using lumped and spatially distributed parameter values. These values are stored in the d-vector θ.

5. Bayesian Inference With Dream: Synthetic Data

We now proceed with fitting of the DTB model parameters using Bayesian inference with DREAM. To be able to benchmark our findings we start with a synthetic record of regolith depth observations created on a regular DEM. This DEM is presented in Figure 2 and simply copies equation (8) to the y direction of the xy plane using 100 different replicates of the topographic surface with $\Delta y = 2$. This DEM is now sampled at random 100 different times (see black dots in Figure 2a) and the regolith depth at each sampled (x, y) location of the grid is computed using
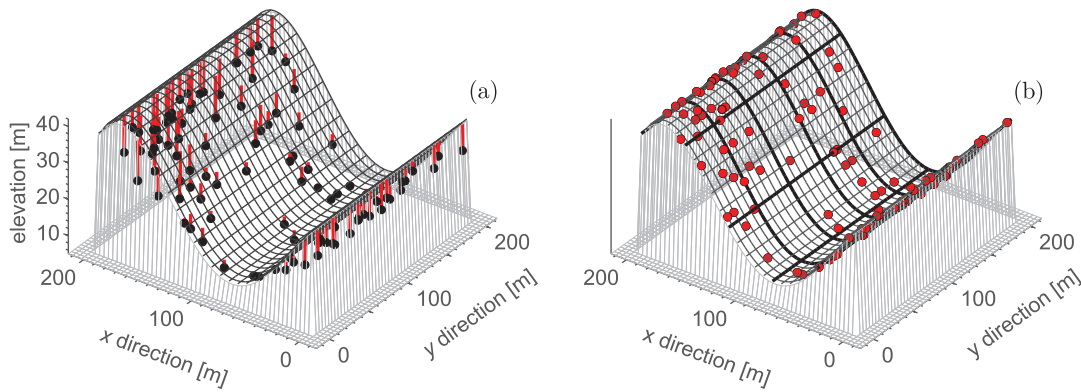
Figure 2. Plot of the synthetic topography of the spatial domain of interest, (a) boreholes (red line) that reach to the bedrock surface (black dot), and (b) measurement locations (red dots). The thin black lines represent the DEM grid with pixels (cells) of 8 × 8 meters, whereas the dark black lines represent the block pattern used in our distributed parameterization of the DTB model.

$$\tilde{h}(x,y) = Z_s(x,y) - \alpha_1 [\alpha_2 + L_d(x,y)/\max(L_d)]^2 + \epsilon_m, \tag{17}$$

where $Z_s(x,y)$ [L] is the elevation of the surface topography at spatial coordinates x, y, and α_1 [L] and α_2 [-] are two coefficients whose values determine the borehole depth, and ϵ_m [L] denotes the measurement data error of the bedrock depth data. Thus, the regolith depth at any location in the DEM is computed by subtracting from the surface elevation the borehole depth and adding a measurement error.

We assume that $\alpha_1 = 8$ and $\alpha_2 = 0.1$ and draw the measurement data error from a normal distribution with $a = 0$ mean and standard deviation $b = 1/2 \hat{\sigma}_{Z_b}$, or $\epsilon_m \sim \mathcal{N}(a, b)$, where $\hat{\sigma}_{Z_b}$ denotes the standard deviation of the $n = 100$ bedrock depth observations before their corruption with a measurement error. Table 3 summarizes the statistical properties of the resulting bedrock depth data set, including sample size and the minimum, maximum, mean, and standard deviation of the regolith thickness. This latter statistic determines the measurement error of the bedrock depth observations, $\hat{\sigma}_{Z_b} = 1.43$ m and provides a benchmark of the "best-fit" attainable by the DTB model (of which more later). The final data set of bedrock depth observations is stored in the n-vector $\tilde{\mathbf{H}} = \{\tilde{h}_1, \ldots, \tilde{h}_n\}$ and is now used to calibrate the DTB model using lumped and spatially distributed parameter values.

5.1. DTB Model With Lumped Parameter Values

The DTB model has four parameters $\theta = \{\Phi, \lambda_1, \lambda_2, S_c\}$ whose values are difficult to be measured directly in the field and hence require calibration against observed bedrock depth data. In the absence of detailed geologic data, we conveniently hypothesize the underlying rock mass to be homogeneous and use spatially invariant values of the DTB parameters, θ. We will revisit this hypothesis in the next section of this paper using spatially distributed parameter values. We adopt the likelihood function of equation (14) and use a multivariate uniform prior distribution for the DTB model parameters. With such noninformative prior, the posterior density in equation (16) is then simply proportional to equation (14) and used herein for inference of the DTB model parameters. The prior ranges of the parameters are listed in Table 4. The minimum and maximum value of parameter Φ are set to 10^{-4} and 10^{-1}, respectively. These ranges are rather wide, and with a bedrock porosity of $\phi = 0.1$ and values for the hydraulic conductivity of consolidated crystalline rocks that range between 10^{-8} and 10^{-13} m/s, gives values of the channel incision rate, C_o of 0.03 to 3 mm/yr. These ranges of C_o are in agreement with values reported in *Rempe and Dietrich* [2014]. The prior ranges of $\lambda_1 \in [0.1, 3]$ and $\lambda_2[1, 20]$ are derived from the results of section 3, and the bounds of $S_c \in [0.8, 1.5]$ are inspired from the literature.

Figure 3 presents a scatter plot matrix of the posterior samples derived with the DREAM

Table 3. Summary Statistics of the Bedrock Depth Observations of the Synthetic and Real-World Data Set Used Herein

Data Set	Minimum [m]	Maximum [m]	Mean [m]	σ^a [m]	n^b
Synthetic	0.13	11.60	4.36	2.97	100
Real world	0.35	14.00	6.20	3.67	137

[a]Standard deviation.
[b]Number of point observations.

Table 4. Prior Uncertainty Ranges of the DTB Parameters for the Artificial and Observed Bedrock Depth Data

Range	Φ	λ_1	λ_2	S_c
Minimum	10^{-4}	0.1	1.0	0.8
Maximum	10^{-1}	3.0	20.0	1.5

algorithm. The main diagonal displays histograms of the marginal distribution of each individual DTB model parameter, whereas the off-diagonal graphs display bivariate scatter plots of the posterior samples. The x axes matches exactly the prior ranges of the parameters (except for the parameter Φ) and the maximum a-posteriori (MAP) solution is separately indicated in each histogram with the blue cross. These parameter values ($\{\theta_{MAP}\} \subset \theta \mathrm{argmax}(|\bar{H})$ are associated with the highest value of the likelihood function of equation (14) of all posterior samples generated by DREAM, and this MAP solution coincides almost perfectly with the posterior median values.

The posterior histogram of the DTB model parameter Φ centers nicely around its MAP solution and follows an approximately normal distribution. The marginal distribution of this parameter occupies a (very) small portion of its uniform prior distribution, which demonstrates that this parameter is very well defined by calibration against the observed (synthetic) bedrock depth data. The posterior histograms of the two bedrock-valley shape parameters, λ_1 and λ_2 are not particularly well identifiable. The marginal distribution of λ_1 in Figure 3f exhibits normality, although the histogram is somewhat skewed to the left and occupies a large part of the prior distribution. The MAP solution of λ_1 between 1 and 2 indicates that the bedrock surface in the valley does not reach the ground surface (see Figure 1). In other words, the valley is mantled with a thin layer of soil. The marginal distribution of parameter λ_2 deviates considerably from normality and is much better described with an uniform distribution. Note that the histogram of λ_2 appears truncated at the upper end by its prior distribution. As the probability mass is distributed mainly at higher values of λ_2, we conclude that the shape of the bedrock surface in the valley follows closely that of the surface topography in the channel. The parameter S_c follows a log-normal distribution and is truncated at the lower boundary of its prior distribution. That relatively low values of S_c are perhaps not that surprising as the artificially generated bedrock depth observations were made close to the ground surface in a relatively steep hillslope. We will revisit the posterior distribution of S_c later in this paper. The bivariate scatter (off-diagonal) plots highlight negligible the presence of some correlation between the DTB parameters. For instance, consider
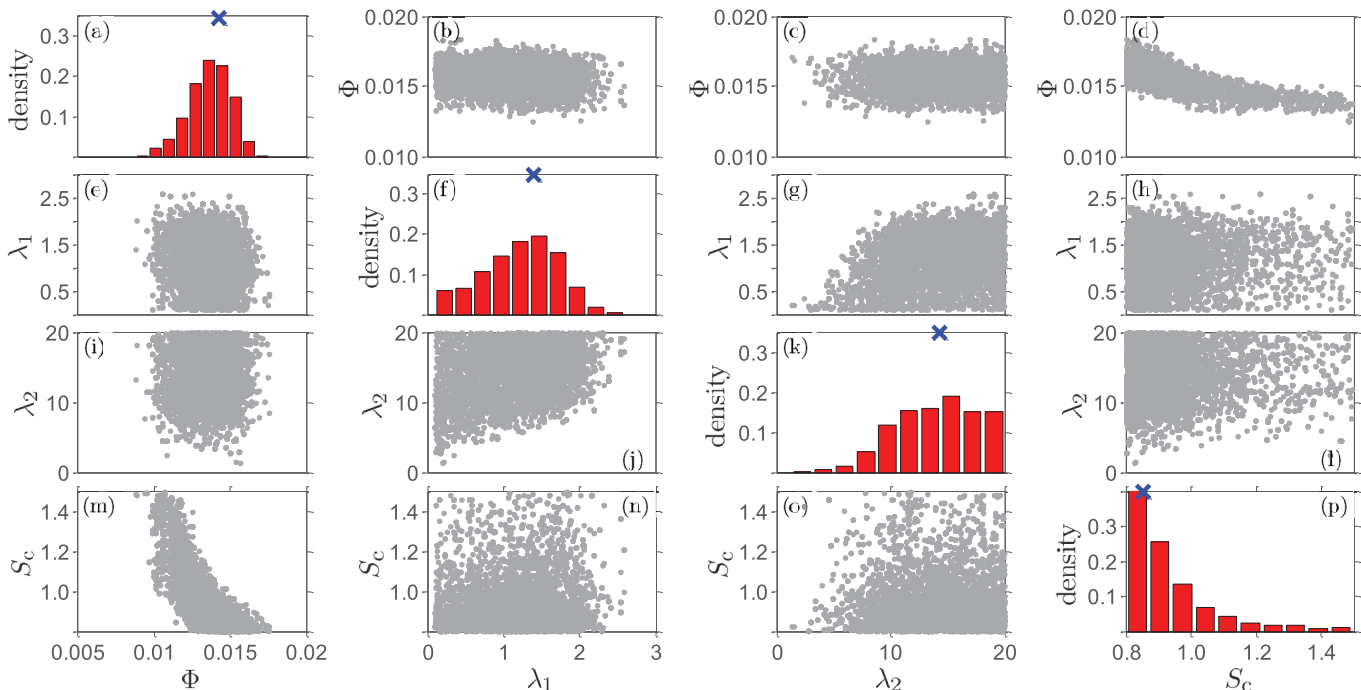

Figure 3. Lumped DTB parameterization: scatter-plot matrix of the posterior samples generated with the DREAM algorithm. The main diagonal plots histograms of the marginal posterior distribution of the DTB model parameters, Φ, λ_1, λ_2, and S_c, respectively, and the off-diagonal graphs present bivariate scatter plots of the posterior samples of the different parameter pairs. The MAP solution (value associated with highest likelihood) is separately indicated in each histogram with the blue cross symbol. The parameters exhibit a negligible correlation by calibration against the observed bedrock depth data.

Table 5. Performance Statistics of the Calibrated DTB Model After Bayesian Inversion With the DREAM Algorithm[a]

Data Set	Case	Dimension (d)	RMSE [m]	ρ	AIC
Synthetic	Lumped	4	1.52	0.86	192.30
	Distributed	7	1.47	0.87	191.74
	Distributed	28	1.40	0.88	221.43
Real world	Lumped	4	1.80	0.83	194.00
	Distributed	5	1.76	0.83	191.10
	Distributed	8	1.76	0.82	193.90

[a]We list separately the results for the synthetic (case-study I: top) and real-world (case study II: bottom) data set of bedrock depth observations using lumped and spatially distributed parameter values. The listed values of the root mean square error (RMSE) and correlation coefficient, ρ pertain to the calibration data set for the synthetic bedrock topography and evaluation data set for the real-world regolith depth observations. The AIC values in the last column are computed with equation (18) using the maximum likelihood (= MAP) values of the parameters derived from the calibration data set.

the (Φ, S_c) scatter plots (top right, bottom left) which depicts a somewhat nonlinear dependency between these two parameters.

The performance of the DTB model is now evaluated using two statistical metrics including the root mean squared error (RMSE) and the Pearson product moment correlation coefficient, or ρ-statistic. Mathematical formulas for both are readily found in statistics textbooks. The RMSE measures the average distance between the observed and simulated bedrock depth data. This statistic has a similar unit as the observations themselves. The lower the value of the RMSE the closer the model predictions to the data. The ρ-statistic measures the strength and direction of a linear relationship between two variables. It is used herein to quantify how well the DTB model predicted bedrock depths fall on the (1:1) line with their observed values. Table 5 summarizes the performance of the DTB model using the posterior mean parameter values. The calibrated DTB model has a ρ-value of 0.86 and RMSE of approximately 1.52 m. This value of the RMSE is much lower than that derived from an uncalibrated DTB model (not shown) and of similar magnitude as the measurement data error, $\hat{\sigma} = 1.43$ m. This latter finding is particularly important and demonstrates the ability of the DTB model to describe accurately the observed bedrock depth data with spatially invariant parameter values.

The assumption of parameter homogeneity is convenient but might not be borne out by the actual properties of the hillslope or watershed which can exhibit significant system heterogeneities at different spatial scales. Much effort would be required to characterize adequately the rock mass properties such as discontinuities, saturated permeability, and porosity for a reasonably sized watershed. The use of spatially distributed parameter values provides a means to account implicitly, and in a relatively simple way, for system heterogeneities that are difficult, or sometimes impossible, to characterize adequately in the field. For example, if the value of the parameter Φ is varied spatially, then the DTB model will assume spatially varying permeability and/or porosity values, given measured values of the channel-incision rate, C_o.

In the next section of this paper, we will investigate the benefits of using a distributed DTB parameterization. This distributed approach is of particular relevance to real-world data sets, but cannot be expected a priori to improve significantly upon the fitting results of our lumped DTB parameterization for the synthetic data set which already achieved posterior RMSE values close to the measurement data error. Any further improvements in quality of fit of the DTB model must be carefully interpreted.

5.2. DTB Model With Spatially Distributed Parameter Values

The use of a distributed parameterization requires some changes to the setup of the DTB model. This is depicted schematically in Figure 4 which summarizes the setup of the DTB model for an invariant (lumped) and variant (distributed) parameterization. The top plot displays the surface of an idealized DEM consisting of P cells (pixels). To simplify notation, we use a single variable, $i = \{1, \ldots, P\}$ to denote the xy coordinates of a DEM cell. The input data of the DTB model in equation (4) differs per grid cell and is stored in the vector, $\mathbf{U}_i = \{\nabla Z_{bi}, L_{di}\}$. If a lumped parameterization of the DTB model is used, then it suffices to use the same parameter values, $\theta = \{\Phi, \lambda_1, \lambda_2, S_c\}$ for each cell of the xy grid. This approach is most convenient and widespread in the geomorphologic literature. A distributed DTB parameterization uses different parameter values for each region of the DEM. This approach increases significantly the dimensionality of the parameter estimation problem and the required CPU-time for DTB calibration. Also, the spatially distributed framework requires the user to define a spatial pattern for each of the model parameters. For example, in Figure 4 we assume a simple block pattern of $r = 16$ equal-sized squares for each of the parameters. Each individual square thus consists of four different grid cells. In a distributed parameterization, the values of the parameters of the first square (top left) are thus assigned to grid cells 1, 2, 9, and 10. After the parameterization of
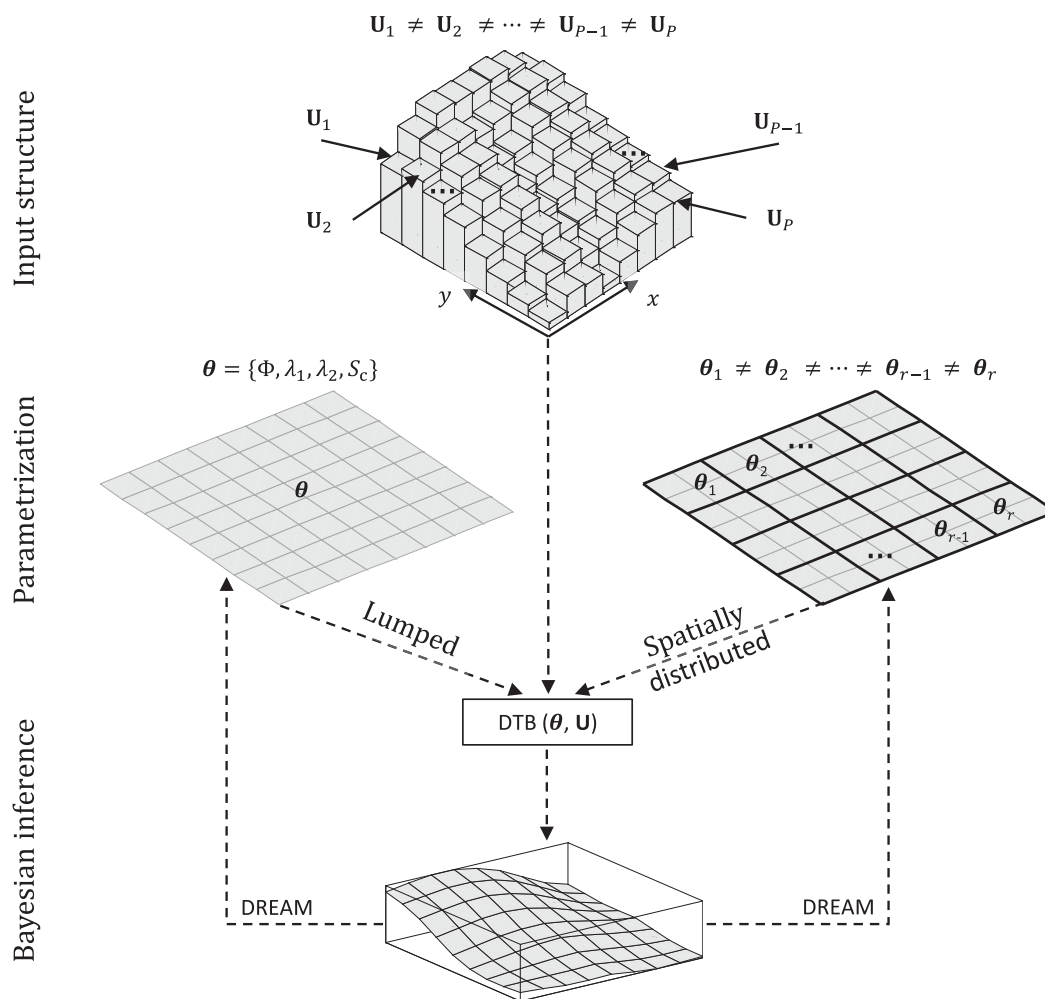
Figure 4. Schematic overview of the DTB modeling framework for a lumped (left) and distributed (right) parameterization of the water-shed. The idealized DEM consists of P different grid cells and each have their own specific vector, $\mathbf{U}_i$, $i=\{1,\ldots,P\}$, of DTB input data consisting of slope gradient and the drainage distance. The lumped (default) DTB model parameterization uses a single realization of the parameter values, $\theta=\{\Phi, \lambda_1, \lambda_2, S_c\}$ for all P grid cells of the DEM. This requires calibration of just a handful of parameters. A distributed parameterization, on the contrary, assumes different parameter values for each grid cell of the DEM. A simple block pattern is used to distribute the DTB parameters over the spatial domain of interest. The DREAM algorithm then proceeds with statistical inference of the model parameters by fitting the model to spatially distributed bedrock depth observations.

the DTB model has been defined, the DREAM algorithm proceeds with statistical inference of the model parameters using distributed observations of the bedrock depth. Both implementations use the same source code of the DTB model but differ in their assignment of the parameter values.

We are now left with the question of how to distribute the values of Φ, λ_1, λ_2, and S_c over the grid domain of interest. Care should be exercised not to use too many parameters in lieu of overfitting. Two main approaches can be used to determine the spatial distribution of the parameter values. The first approach fixes a priori the spatial structure of the parameters and then determines the actual values of this pattern by fitting the DTB model to the observed bedrock depth data. An example of this approach is found in Figure 2b for a block pattern and this design is used herein for illustrative purposes. One can also link the spatial structure of θ to properties of the DEM to guide the spatial structure of the parameter values. The topographic position index [*Tesfa et al.*, 2009; *Reu et al.*, 2013] can be used as guiding metric to determine the spatial structure of the parameters. This approach fixes a priori the spatial structure of the DTB parameters, and this pattern might therefore not necessarily honor the underlying bedrock heterogeneity. Alternatively, one can use so-called model-reduction techniques and let the actual regolith depth observations determine simultaneously the pattern and values of the DTB model parameters. Examples of such model-
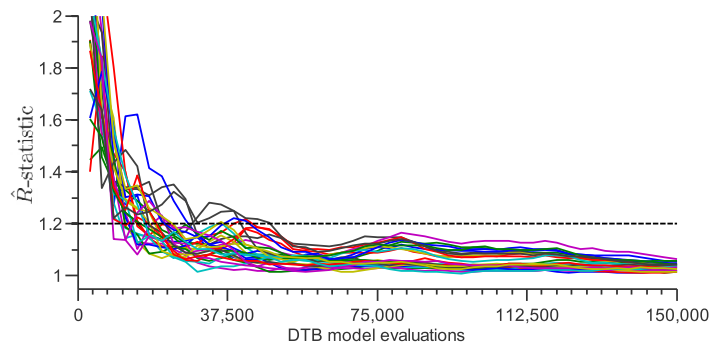
Figure 5. Distributed calibration case: evolution of the $\hat{R}$-convergence diagnostic of *Gelman and Rubin* [1992] for each individual parameter of the DTB model ($d = 28$). Each parameter is coded with a different color. The dashed black line depicts the default threshold used to diagnose convergence to a limiting distribution.

reduction approaches include the discrete cosine transform [*Linde and Vrugt*, 2013; *Lochbühler et al.*, 2015], wavelet transform [*Davis and Li*, 2011; *Jafarpour*, 2011], and singular value decomposition [*Laloy et al.*, 2012; *Oware et al.*, 2013]. We have tested this alternative approach in the present study but found little improvements in the quality of fit of the DTB model (not shown).

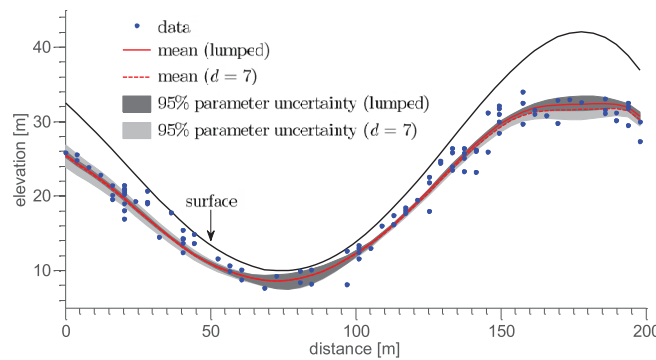We now illustrate the results of the DTB model using two different distributed parameterizations of Φ. In our first trial, we divide the *xy* plane of the DEM into $r = 4$ equal-sized rectangles and assume a different value of Φ for each oblong. The remaining parameters (λ_1, λ_2, and S_c) continue to take on a single lumped value that pertains to the entire spatial domain (Figure 4). The parameter dimensionality has increased from $d = 4$ in the first case study to $d = 7$ in the present study. In the second trial, we increase the number of square blocks for the parameter Φ to 25 as shown in Figure 2b. This then leaves us with a total of $d = 28$ parameter values that require calibration against the observed bedrock depth data using the DREAM algorithm.

Figure 5 displays trace plots of the $\hat{R}$-statistic of *Gelman and Rubin* [1992] for each of the model parameters ($d = 28$) using the last 50% of the samples stored in each of the $N = 15$ Markov chains. This convergence diagnostic compares the within-chain and between-chain variance of each parameter $j = \{1, \ldots, d\}$ of the DTB model. The different parameters are color coded. Convergence to a stationary distribution can be declared if the $\hat{R}_j$-statistic of each of the $d = 28$ parameters drops below the critical value of 1.2. Results demonstrate that about 50,000 DTB model evaluations are required for DREAM to converge successfully to a stationary distribution and satisfy the convergence threshold. This rather large number of model evaluations involves a rather low computational effort due to the relative CPU efficiency of the DTB model. If desired, each Markov chain sampled with DREAM can be evaluated on a different processor permitting inference of CPU-demanding transient models. Most of the DTB parameters appear well defined by calibration to the observed bedrock depth data (not shown). We will investigate this further in the next section of this paper using real-world observations of the depth to bedrock.

To determine which of the model complexities is best supported by the available regolith depth data, we use Akaike's Information Criterion (AIC) [*Akaike*, 1974]. This metric takes into consideration model complexity (= parameter dimensionality) and the goodness of fit. Hence, AIC provides a means for model selection. The value of AIC is computed as follows

$$\text{AIC} = -2\ln\left\{L(\theta_{\text{MAP}}|\tilde{\mathbf{H}})\right\} + 2d, \tag{18}$$

where $L(\theta_{\text{MAP}}|\tilde{\mathbf{H}})$ is the maximum value of the likelihood function derived from the MAP (= best) parameter values. Given a collection of models for the data, AIC estimates the quality of each model, relative to each of the other models. Models with lower AIC values are preferred statistically. Note, AIC does not give a warning if all models fit poorly, and hence this metric has to be interpreted jointly with other model performance criteria.

Table 5 summarizes the performance of the DTB model with a distributed parameterization of Φ. The RMSE has reduced from 1.52 (lumped: $d = 4$) to 1.47 m (distributed: $d = 7$) and the ρ-statistic has slightly increased from 0.86 to 0.87. The results of the second trial ($d = 28$) show a further reduction of the RMSE and another increase of the ρ-statistic. In fact, the RMSE is now slightly lower than the (Gaussian) measurement error of $\hat{\sigma}_{Z_b} = 1.43$ used to corrupt the $n = 100$ bedrock depth observations.

To understand whether these improvements in fit are statistically warranted, we also list, in the last column of Table 5, the AIC values for each of the three DTB model parameterizations. The lowest value of the AIC is

Figure 6. Lumped and distributed calibration case: simulated bedrock surface of the DTB model for the lumped and distributed parameter case. The mean posterior solution is indicated with the solid (lumped) and dashed (distributed) red line, respectively, and the light and dark gray region represent the 95% prediction intervals due to parameter uncertainty for each case. The observed bedrock depth data are separately indicated with the blue dots.

found for the first distributed parameter case with $d = 7$. This constitutes a marginal improvement over the value of AIC = 192.30 for the lumped parameterization with $d = 4$. This suggest that Φ is better characterized with the use of spatially distributed values. The second distributed case with $d = 28$ parameters, albeit having the lowest value of the RMSE and highest ρ-statistic, has a value of AIC = 221.43 which is much larger than the other two model parameterizations. These results caution against the use of an excessive number of parameters due to potential problems of overfitting. Indeed, a lumped or a spatially distributed parameterization ($d = 7$) of the DTB model suffices for this synthetic data set, and any further improvements in fit are not warranted by the available bedrock depth observations.

Thus far, we have focused our attention on the posterior parameter distributions of the DTB model and summary statistics of the quality of fit of the mean solution. We now turn our attention to the simulated output of the DTB model and plot in Figure 6 the bedrock surface of the posterior mean solution of the lumped (solid red) and distributed (dashed red) parameterization for a synthetic hillslope transect. The dark and light gray regions display the 95% prediction uncertainty ranges of the simulated bedrock depths using lumped ($d = 4$) and distributed ($d = 7$) parameter values, respectively. The topographic surface is indicated with the black line, and the observed regolith depth data are separately indicated with the solid blue dots. The posterior mean simulation of the lumped and distributed parameter case appears rather similar (as expected from Table 5) and tracks closely the observed bedrock depth data. The simulated bedrock surface is much smoother than expected from the observed data and does not fit the malicious small-scale variations of the regolith thickness induced by the measurement error. These erroneous small-scale variations in the bedrock depth appear to be largest at the side slope, generating a thin regolith thickness in this region. This might explain why the marginal distribution of S_c in Figure 3p favors relatively small values. The prediction uncertainty of the lumped DTB calibration is much smaller than its counterpart derived from a distributed parameterization, except at the drainage channel. This is a common finding and highlights a trade-off between model complexity (=parameter dimensionality) and prediction uncertainty. We will discuss later the implications of this bedrock prediction uncertainty on hydrologic and geotechnical analysis.

6. Bayesian Inference With Dream: Application to the Papagaio River Basin

We now apply the DTB model to a real-world data set. In the next sections, we describe the experimental field site, data collection, and present the results of DTB model calibration and evaluation for a lumped and distributed parameter case.

6.1. Experimental Field Site

Field investigations were carried out in two adjacent watersheds in the Papagaio river basin in Rio de Janeiro, Brazil. These two watersheds have been studied extensively by many different authors in the literature after mass movement occurred in 1996 [*Guimarães et al.*, 2003; *Fernandes et al.*, 2004; *Vieira and Fernandes*, 2004; *Gomes et al.*, 2008, 2013] (among others). A detailed description of the field site appears in these cited publications, and thus will not be repeated herein. The geographic location of the field sites is depicted with a red cross in Figure 7 which also presents (left hand side) the topography of the two experimental basins. The white dots signify the measurement locations, and the hillslope transects **AA**' and **BB**'
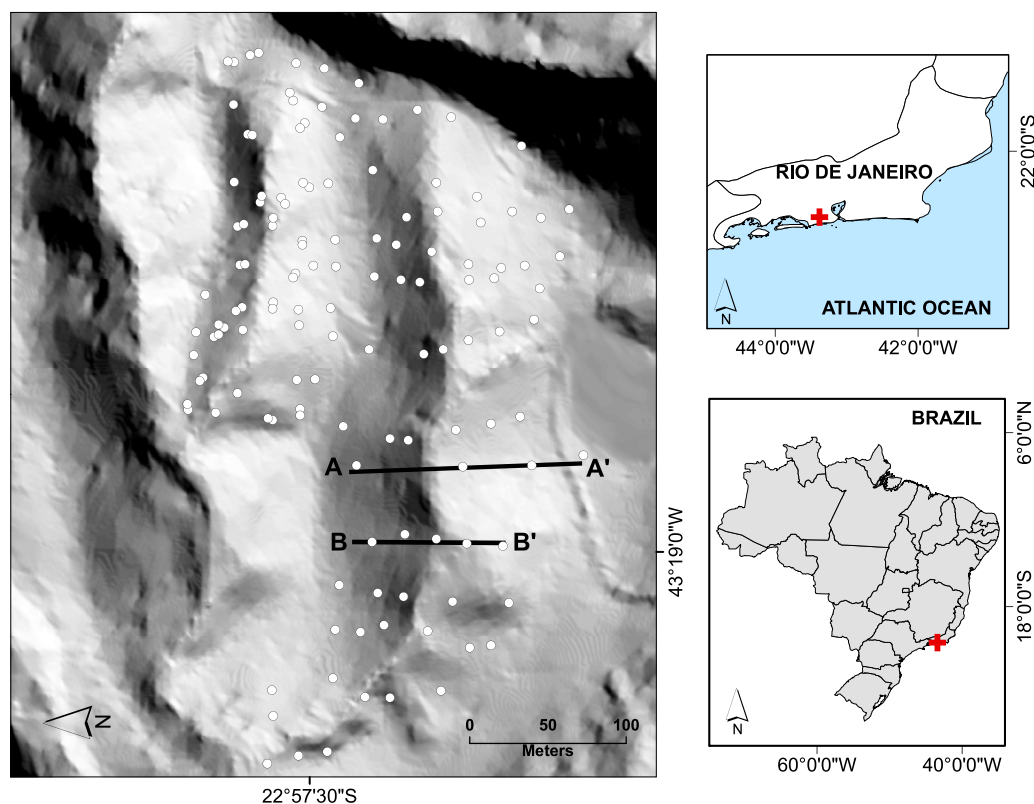
Figure 7. (right) Geographic overview and (left) shaded relief image of the PRB experimental field site in Rio de Janeiro, Brazil. The PRB field site is indicated with a red cross. The white circles (left) denote the measurement locations of the regolith depth observations using a dynamic cone penetrometer. The transect **AA'** is used to demonstrate the effects of DEM smoothing. The transect **BB'** is a cross-section in the south subbasin and used herein to compare the simulated bedrock profile against observations of the regolith depth to unweathered bedrock.

are of particular interest herein. The elevation in the surveyed region ranges between 190 and 360 m above sea level with slopes that vary between 0 and 57°.

The local bedrock consists of high-grade metamorphic rocks (Archer gneiss is most frequent) with granite intrusions of coarse-medium granular texture [*Fernandes et al.*, 2004; *Vieira and Fernandes*, 2004]. Human impact in the region has been limited to a few small areas used for agricultural activities [*Gomes et al.*, 2008] and the vegetation (Atlantic forest) has been preserved in most parts of the basin. DTB observations were made at $n = 137$ different locations in the two watersheds using a light dynamic cone penetrometer (DPL). These locations were carefully selected to maximize information retrieval about the underlying bedrock surface and include a rich sample of convex, concave, planar, convergent, and divergent slopes. Statistical properties of the regolith depth observations are listed in Table 3.

Our definition of soil-bedrock interface using DPL tests follows many approaches published in the literature [*Kosugi et al.*, 2006, 2009; *Fujimoto et al.*, 2008; *Ohnuki et al.*, 2008; *Askarinejad et al.*, 2012; *Wiegand et al.*, 2013; *Athapaththu et al.*, 2014; *Liang and Uchida*, 2014]. The test consists of a steel cone (10 cm² area) that is driven into the soil by the falling energy of a 10 kg hammer. The hammer transmits an exact amount of energy (of a fixed height of 50 cm) to a set of 1 m length steel rods. With the hammer impact, the set of rods penetrates vertically and number of blows to advance 10 cm is computed. The definition of the regolith depth depends on DPL type and site-specific conditions. Each one of the cited publications above have adopted a different approach to measure bedrock topography. In this paper, we implement the following procedure to measure the bedrock-depth surface: (1) 100 blows to advance 10 cm; (2) 80 or more blows to advance three consecutive segments of 10 cm; (3) 60 or more blows to advance five consecutive segments of 10 cm; and (4) depth greater than 12–13 m. DPL has a limitation to achieve depths greater than 13 m, since the extraction of the rods may be compromised. However, our field experiments demonstrated that
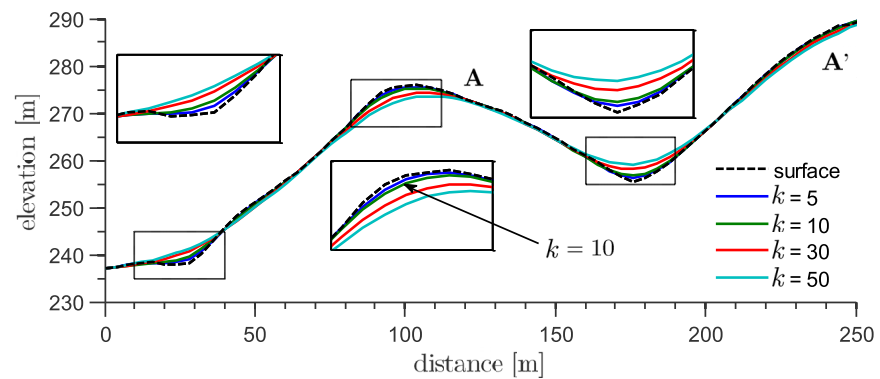
Figure 8. The effect of the number of iterations of the smoother algorithm on the topographic surface. The large black rectangles are zoomed insets of the smaller rectangles of the footslope (depositional area) and sideslope (steepest gradient). Ten iterations are deemed sufficient to remove the small topographic defects of the DEM.

measured regolith depth was predominantly in the range between 0 and 13 m. What is more, our criteria used to define the soil-bedrock boundary is consistent with approaches adopted in the literature.

The smallest of the two experimental watersheds was used primarily to study small-scale variations in the depth to bedrock. This requires the use of neighboring boreholes that measure DTB within a few meters of each other. The southerly and larger watershed was populated more uniformly with different boreholes to investigate more deeply the bedrock surface along a hillslope. This difference in objective is readily apparent in the areal view of the two catchments in Figure 7. The borehole pattern of the larger watershed in the south appears much more uniform and organized than its counterpart from the northerly watershed (left), which contains many more adjacent boreholes. A differential GPS system was used to determine as accurately and consistently as possible the {x, y, z} location of each borehole. We estimate the remaining location error to be on the order of 0.5 m for all the $n = 137$ different boreholes.

6.2. Model Input Data

The topographic surface is one of the most important input variables of the DTB model. Some correction of this surface is usually required to remove small-scale imperfections arising from (among others) three throw, animal burrows, and LiDAR measurement errors [*Pelletier and Rasmussen*, 2009]. Such DEM errors can otherwise corrupt the results of models which rely heavily on the first and second-order derivative of the topography (slope and curvature of DEM) in their calculation of the soil/bedrock depths. Indeed, when a DEM is differentiated, the small-scale variability of the topographic data is amplified relative to large-scale topographic variations that define the overall shape of the hillslope.

Even the most accurate and advanced topographic surveying methods such as high-resolution LiDAR exhibit measurement errors that can introduce small-scale defects in the DEM and deteriorate the simulated bedrock depths by introducing erratic and malicious spikes and dips in first and higher-order topographic derivatives used by different models. A generally practiced method to avoid this issue is a smoothing approach [*Saco et al.*, 2006; *Pelletier and Rasmussen*, 2009]. We here smooth the DEM prior to application of the DTB model using

$$Z_{i,j}^k = \left[Z_{i,j}^{k-1} + w \left(Z_{i,j-1}^{k-1} + Z_{i,j+1}^{k-1} + Z_{i-1,j}^{k-1} + Z_{i+1,j}^{k-1} \right) \right] \Big/ (1+4w), \tag{19}$$

where $Z_{i,j}$ = elevation of a spatial location given by coordinates i and j [L]; k = iteration; and w = empirical weight [-]. The degree of smoothing can be controlled by the iteration number k and by $w \in (0, 1]$. The exact value of the weight is not particularly important as the degree of smoothing can be controlled by iteration number. The smaller the value of the weight the more iterations are required to reach a certain smoothed topography. The number of iterations required to remove small-scale topographic imperfections depends on the accuracy of the LiDAR observations, and is thus data set dependent.

To better understand how the number of iterations affects the smoothed topographic, please consider Figure 8 which plots the outcome of equation (19) for different values of k and $w = 0.2$ using a cross section of the DEM of the PRB. The plot shows the topographic surface for values of $k = 5$ (blue), $k = 10$ (green), $k = 30$
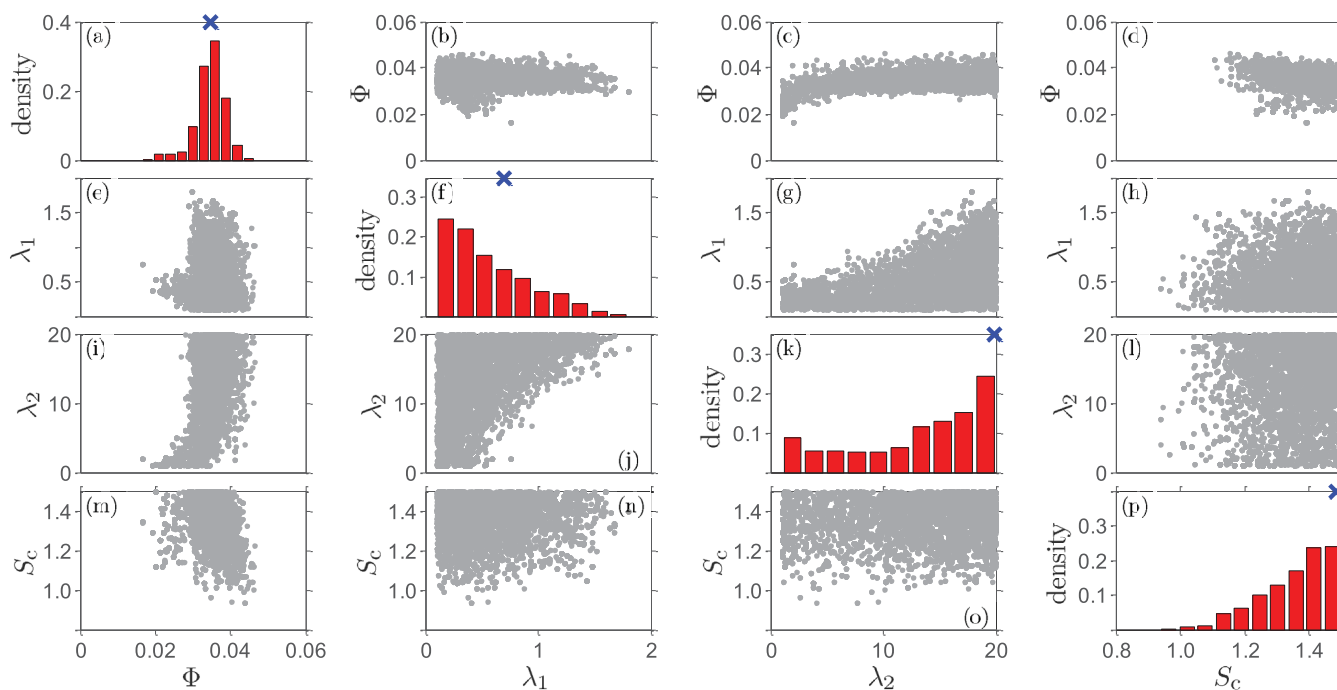
Figure 9. Lumped DTB parameterization: scatter-plot matrix of the posterior samples generated with the DREAM algorithm. The main diagonal plots histograms of the marginal posterior distribution of the DTB model parameters, Φ, λ_1, λ_2, and S_c respectively, and the off-diagonal graphs present scatter plots of the posterior samples of the different parameter pairs. The MAP solution (solution with highest likelihood) is separately indicated in the histograms with the blue cross symbol. The parameters pairs exhibit a negligible correlation.

(red), and $k = 50$ (cyan). The original LiDAR measured (nonsmoothed) surface is separately indicated with the dashed black line. The large black rectangles are zoomed insets of the smaller rectangles of the foot slope (depositional area) and sideslope (steepest gradient) and much better demonstrate the effect of the different iterations on the topographic surface. A few iterations (5–10) with the smoothing kernel of equation (19) is sufficient to remove the small-scale defects (roughness) so clearly visible in the insets but does not affect the main properties of the DEM. The use of a larger number of iterations ($k > 10$) compromises unnecessarily the DEM and introduces topographic discrepancies in the drainage and hilltop regions of the hillslope. In summary, a value of $k \in [5, 10]$ is sufficient to correct for small-scale topographic imperfections and maintains the overall integrity and characteristics of the measured DEM. For other values of $w \in (0, 1]$, the same analysis can be repeated to determine a suitable value for k.

Different approaches have been used in the literature to remove the pit-and-mound topography captured by LiDAR DEM but also retain the hillslope scale pattern [*Saco et al.*, 2006; *Pelletier and Rasmussen*, 2009]. Recent studies have attempted to extract relevant scales for smoothing high-resolution surfaces [*Roering et al.*, 2010; *Hurst et al.*, 2012]. However, a discussion about different smoothing methods is outside the scope of the present paper and we refer to these publications for further information. We now use the smoothed DEM as input to DTB model and fit the model against observed bedrock depth data using a lumped and distributed parameterization with the DREAM algorithm.

6.3. DTB Model With Lumped Parameter Values

The method proposed in section 5.1 is now applied to the borehole observations at the experimental site. The bedrock data set is split randomly into two parts, designated for DTB-model calibration (75%) and evaluation (25%). The observations that were affected by tree roots and boulders were removed from the data set. A pixel size of the DEM of 4 m was deemed an acceptable trade-off between model accuracy and computational efficiency. We now estimate the posterior distribution of the DTB model parameters, $\boldsymbol{\theta} = \{\Phi, \lambda_1, \lambda_2, S_c\}$ using Bayesian inference with DREAM. The prior ranges for the parameters are listed in Table 4. We now discuss the results.

Figure 9 presents a scatter plot matrix of the posterior samples derived from DREAM. The graphs on the main diagonal present marginal distributions of each of the parameters, whereas the off-diagonal elements
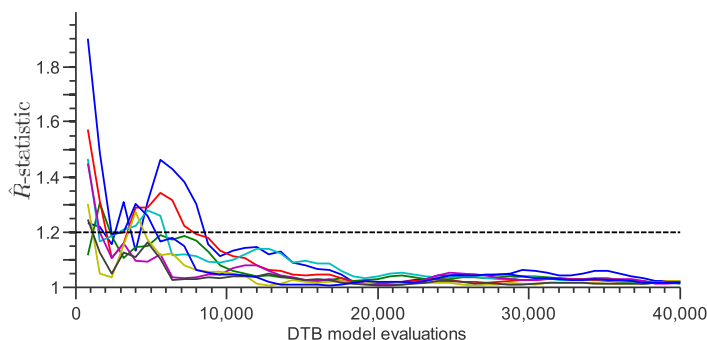
Figure 10. Distributed calibration case: trace plot of the $\hat{R}$-convergence diagnostic of *Gelman and Rubin* [1992] for each individual parameter of the DTB model ($d = 8$). Each parameter is coded with a different color. The dashed black line depicts the default threshold used to diagnose convergence to a limiting distribution. About 10,000 model evaluations are needed with DREAM to converge to the posterior distribution.

display bivariate scatter plots of the posterior samples. The posterior distribution of the parameter Φ follows closely a normal distribution with median posterior solution that is in excellent agreement with the MAP value, separately indicated in the histogram with the blue cross symbol (A). The posterior histogram of Φ has many elements in common with its counterpart derived in the synthetic study case (Figure 9a). Indeed, the marginal distribution extends only a small portion of the uniform prior distribution, which demonstrates that this parameter is well defined by calibration against the real-world bedrock depth data. The marginal distributions of the other three parameters occupy almost their entire prior distribution, which suggest that these parameters are poorly defined by calibration against our bedrock depth observations. The relatively low values of the parameter λ_1 (including the MAP value) suggest that the bedrock is close to the surface in the channel zone with a thin soil mantle overlying a weathered bedrock zone (Figure 9f). The high MAP value for λ_2 (Figure 9k) signifies that the bedrock valley topography approximates a smooth concave shape (see Figure 1). The marginal distribution of parameter S_c is quite different from its synthetic case (Figure 9p). Indeed, S_c now attains much higher values, demonstrating the presence of a much thicker regolith zone underneath steep slopes. The bivariate scatter plots (off-diagonal) highlight the presence of some negligible correlation between the DTB parameters, Φ and λ_2 and Φ and S_c as in section 5.1.

The posterior mean parameter values derived from the calibration are now used to determine the performance of the DTB model on the independent evaluation data set. The performance of the DTB model is summarized in Table 5. The listed value of the RMSE of 1.80 m and the ρ-statistic of 0.83 can be considered acceptable for the PRB experimental watershed. These performance metrics might be improved upon if a distributed parameterization of the DTB model is used. We therefore turn our attention again to the assumption that the parameter Φ might contain information about rock heterogeneity not explicitly accounted for in the DTB model formulation. We discuss the results of such distributed parameterization in the next section.

6.4. DTB Model With Spatially Distributed Parameter Values

In a previous section of this paper, we have shown (see Figure 1) that the DTB model simulates a smooth bedrock surface from the hilltop to the drainage channel in the valley. Such regular surface does not do justice to the rather dynamic variations of the regolith thickness at different experimental sites in Rio de Janeiro. This DTB variability is partly explained by measurement errors of the dynamic cone penetrometer but cannot be described and mimicked accurately with an analytic solution. The assumptions of the DTB model are convenient in deriving analytic solutions of the bedrock surface but might not characterize adequately three-dimensional topographic effects arising from ridge and valley topography and vertical or lateral heterogeneities, particularly the K/ϕ relation [*Rempe and Dietrich*, 2014]. What is more, the channel incision rate, C_o is unlikely to be constant over large timescales, due to (among others) a variably bedrock resistance, lateral movement of the channel, and internal dynamics of stream capture at the PRB field site. Furthermore, the bedrock is assumed to be spatially homogeneous and rock mass discontinuities are ignored. These processes (and properties) are very difficult to characterize adequately with an analytic solution, and instead warrants numerical modeling of the bedrock depth.

We now discuss the results of the DTB model for two different distributed parameter cases. In the first trial, a different value of Φ is assumed for each sub watershed of the PRB, and the other three parameters (λ_1, λ_2, and S_c) assume lumped values over the domain of interest (Figure 4). This involves the inference of $d = 5$ parameters. In the second trial, all four DTB-model parameters are varied per subcatchment within the PRB,
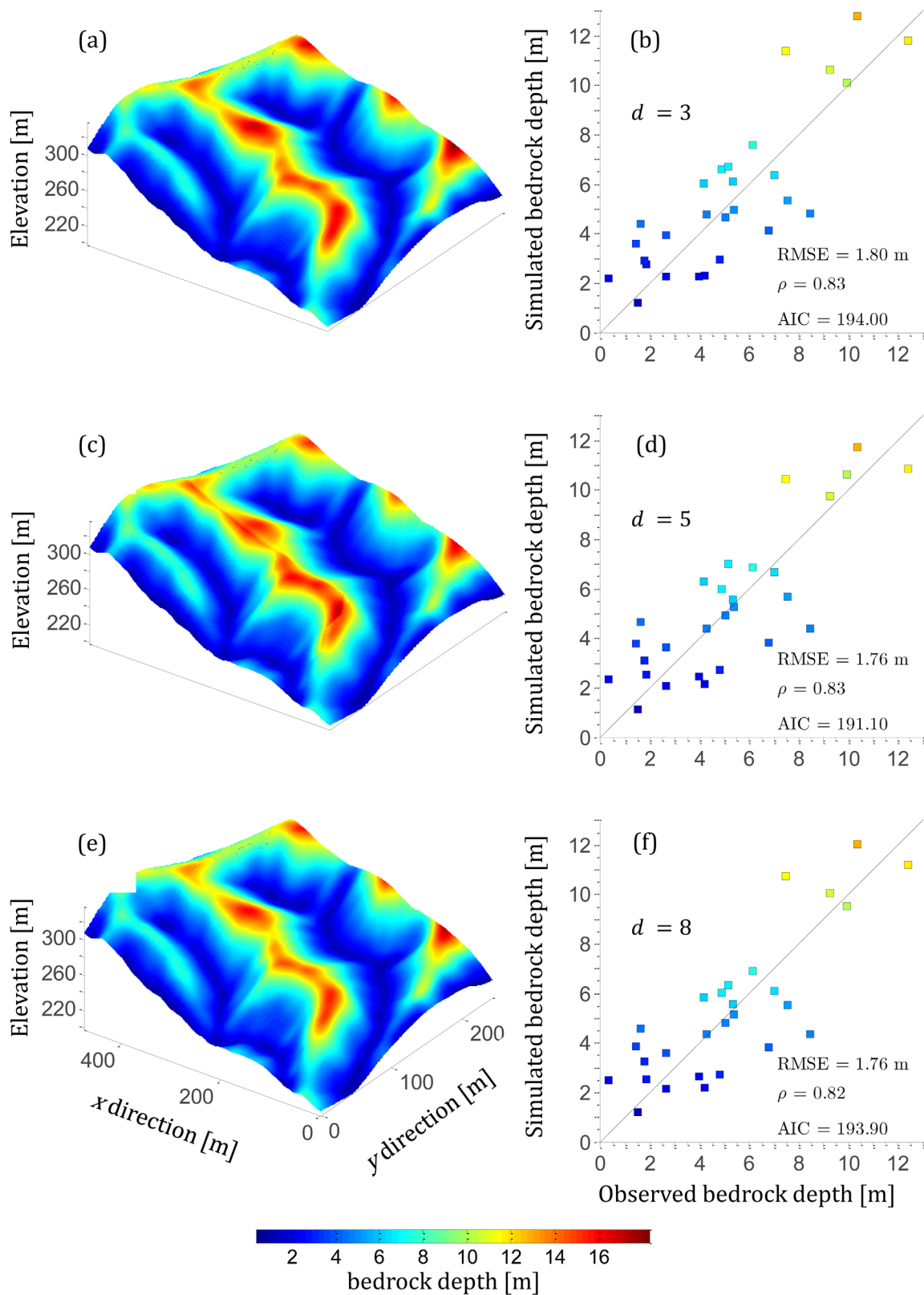
Figure 11. Lumped and distributed calibration case: spatial distribution of the regolith thickness predicted at the PRB experimental watershed using a (a) lumped and (c,e) distributed parameterization. The DTB model predicts deep soils at the hilltop and relatively thin weathered zones in the channel, a result which is in agreement with regolith depth observations at the PRB and field expertise of hillslopes in Rio de Janeiro. The bivariate scatter plots at the right hand side compare the observed and simulated bedrock depths of the evaluation data set of the PRB. Summary statistics of the goodness-of-fit (RMSE, ρ and AIC) are listed in each plot along with the number of model parameters, d. The color coding of these regression plots matches exactly that of the bedrock depth maps.
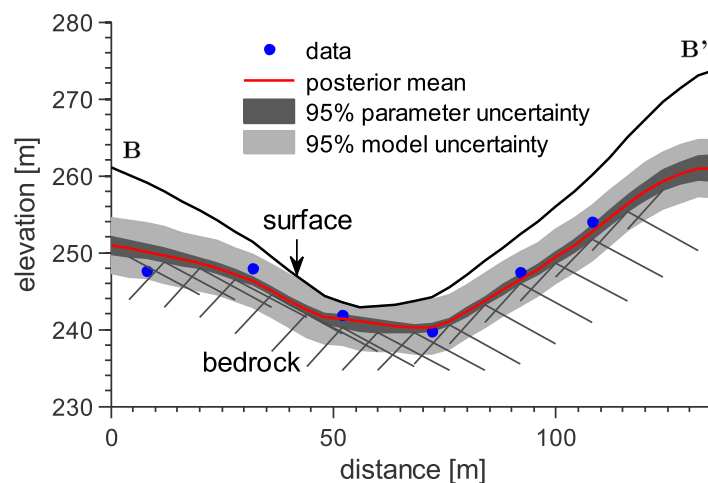
Figure 12. Distributed calibration case: simulated DTB bedrock surface of the posterior mean solution (solid red line) derived from DREAM for the transect **BB**' at the PRB experimental watershed. The dark and light gray region plots the 95% prediction intervals due to the parameter and total simulation uncertainty. The topographic surface is indicated with the black solid line, and the observed regolith depth data are separately indicated with the blue dots.

thereby increasing further the model complexity to $d = 8$. Figure 10 presents the evolution of the sampled $\hat{R}$-values for each DTB model parameters of the distributed parameterization with $d = 8$. About 10,000 DTB model evaluations are required for DREAM to converge successfully to a stationary distribution. This requires a few minutes of calculation on a standard laptop computer. Parallel computing can be used to reduce further the CPU budget.

Table 5 summarizes the performance statistics of the two distributed parameterizations for the evaluation data set. The listed RMSE and ρ-statistics appear very similar with RMSE that has decreased from 1.80 m for the lumped case to 1.76 m for both distributed parameterizations. The ρ-statistic appears rather unaffected and actually has deteriorated somewhat from 0.83 to 0.82 when the number of parameters is increased beyond four (lumped case) or five (first distributed case). The distributed parameterization of the DTB model with $d = 5$ receives the lowest value of the AIC metric, and is thus most supported by the available soil depth data. This value of 191.10 is somewhat lower than its counterpart of 194.00 and 193.90 for the lumped and most distributed parameter case, respectively. Altogether, we conclude that the distributed parameterization with $d = 5$ is statistically preferred.

We now plot in Figure 11 the DTB simulated regolith thicknesses at the PRB experimental watershed using the mean posterior solution of the lumped (A: $d = 4$) and distributed parameterizations (C: $d = 5$; E: $d = 8$). To simplify graphical interpretation, a common color bar is used for all three calibration cases. The scatter plots at the right hand side compare the observed and simulated regolith depth values at the different measurement locations. The solid black line is used to denote the identity or 1:1 line. The color coding in these regression plots matches the color bar used in the figures at the left hand side. The simulated bedrock depth maps of the different calibration cases appear very similar and exhibit only small differences if a distributed parameterization is used. The DTB model predicts a smooth topography from the hilltop (thick regolith) to the drainage channel (thin or even exposed rock), a pattern that agrees well with field observations. These results are in agreement with theory [*Rempe and Dietrich*, 2014; *Clair et al.*, 2015] and field expertise [*Liang and Uchida*, 2014; *Kim et al.*, 2015] for a geologically similar environment with steep slopes on a granitic rock mass, and provides support for the claim that the DTB model gives an adequate description of the bedrock surface at the PRB field site.

We conclude this section with Figure 12, which plots the DTB simulated bedrock profile of the mean posterior solution for the **BB**' transect (Figure 7) using the distributed ($d = 5$) parameterization. The topographic surface is indicated with the black line and the observed bedrock depth data are indicated separately with a blue dot. The dark gray region represents the 95% confidence intervals of the output prediction due to parameter uncertainty, whereas the light gray region denotes the corresponding total prediction uncertainty. The simulated posterior mean bedrock surface (solid red line) appears rather smooth and fits nicely the observed bedrock depth observations. The 95% parameter uncertainty bounds appear relatively small and track closely the observed regolith depth data. The total (model + parameter) 95% prediction uncertainty intervals are rather large and encompass the observations. The different DTB model parameterizations predict a very similar posterior mean bedrock depth surface (not shown), but the prediction uncertainty increases (as expected) with increasing dimensionality of the parameter space.

7. Discussion

The Bayesian inversion framework used herein enables synthesis of geomorphic models with spatially distributed field observations. This approach uses MCMC simulation with DREAM to search efficiently the model parameter space in pursuit of so-called posterior samples that honor best the observed data. The quality of fit is quantified by a likelihood function which takes into explicit account the calibration measurement data error. A prior distribution can be used to constrain the ranges of each parameter and/or to favor values in better agreement with yet available geologic data. The posterior samples of DREAM are then visualized using marginal distributions and pairs of bivariate scatter plots. These plots can be used to assess parameter sensitivity and correlation. Predictive uncertainty can be assessed by evaluating the model with each posterior parameter solution. The posterior mean simulation can then be compared to validation data to benchmark the performance of the model and help verify the main assumptions and equations it is based on. This step is an integral part of the scientific method and key to model (hypothesis) refinement.

The DREAM algorithm is designed specifically to solve for the target distribution in high-dimensional parameter spaces. Parameters whose marginal distribution is relatively tight appear well resolved by the available data. If, on the contrary, the marginal distribution occupies a large portion of the prior distribution, then the parameter cannot be constrained by the calibration data and can be classified as insensitive. The use of spatially distributed parameter values provides a means to account implicitly, and in a relatively simple way, for system heterogeneities that are difficult, or sometimes impossible, to characterize adequately in the field. For example, the DTB model can simulate spatially varying $\phi C_o / K$ if the value of Φ is varied over the watershed of interest. One should be particularly careful however not to use too many distributed parameters to characterize spatially the geomorhic processes and bedrock properties of the watershed of interest as this increases significantly the chances of overfitting. An example of this was given in the first case study involving synthetically generated bedrock depth observations. The closest match with the bedrock data is achieved with a distributed implementation of the DTB-model involving inference of $d = 28$ parameters. The RMSE of this parameterization (1.40 m) is considerably lower than its counterpart of 1.52 m derived from a lumped calibration, nonetheless a comparison of their AIC values (221.43 versus 192.30) suggests that the lumped parameterization is preferred statistically. Thus among competing hypothesis the one with the lowest value of the AIC should be selected. This principle of parsimony is also known as Occam's razor. Indeed, in both our case studies, the simplest distributed DTB-model parameterization ($d = 5$ for the real-world case) is most supported by the available regolith depth data.

Bayesian analysis coupled with MCMC simulation has several key advantages over standard optimization approaches, one of which is the explicitly characterization of model simulation (prediction) uncertainty. The depth to bedrock, for instance, is a key input variable in hydromechanical and geotechnical studies, but without underlying estimates of uncertainty, this boundary is treated instead as a fixed entity in slope stability analysis and debris-flow studies [*Guimarães et al.*, 2003; *Fernandes et al.*, 2004; *Gomes et al.*, 2008, 2013]. As the posterior mean simulation of the bedrock depth underneath the hillslope or watershed was shown to be in excellent agreement with the observed data, the DTB model output should improve considerably simulation of large-scale shallow landslides and debris-flow events [*Gomes et al.*, 2013]. What is more, we can also propagate forward the bedrock depth uncertainty through hydromechanical models to quantify prediction intervals of key output variables such as landslide potential and factor of safety. The availability of an accurate bedrock depth map also makes it easier to characterize adequately the impact of soil hydraulic and soil strength properties on slope stability. Previous work at the PRB published in *Guimarães et al.* [2003] treated bedrock topography and soil cohesion as a single variable-controlling shallow landslides.

A lumped parameterization of the DTB model is warranted for a sparse data set of regolith depth observations. The number of degrees of freedom, $df = n - d$, then remains sufficiently large to minimize the chances of overfitting. If a sufficiently large number of bedrock depth measurements is available, then a distributed DTB model parameterization can be used. The most promising results for the PRB were derived if the parameter Φ is varied spatially per subcatchment. The parameter S_c enables simulation of varying bedrock depths along the hillslope and allows the DTB model as proposed herein to reproduce accurately the presence of thin soils and/or exposed rock at the steep slopes in the upland portion of the PRB. The bedrock-valley morphology in the DTB model is controlled by the variable Λ and inference of its parameters λ_1 and λ_2 allows simulation of many different shapes and depths of the bedrock surface underneath the drainage channel.

In this paper, we have used spatially distributed observations of the bedrock depth as a calibration target. This integrated variable summarizes the cumulative history of a myriad of different geologic processes such as climate cycles, internal dynamic, episodic instabilities (mass movements), variable resistant rock mass, and nonuniform channel incision [*Rempe and Dietrich*, 2014]. These processes act together in the watershed, and their complex (nonlinear) relationships with surface topography, soil, and/or rock mass properties give rise to a spatially variable bedrock depth. By using observations of the bedrock depth at different locations in the watershed, we can constrain sufficiently the parameters (and output) of the DTB model, yet other data types are needed to verify whether the processes simulated by the model are adequately described. Without such data, it will be very difficult to benchmark the adequacy of the different components of the DTB-model in pursuit of epistemic errors. It is not particularly difficult to adapt the likelihood function of equation (14) to include other calibration data types as well.

If the main application of our DTB model is to produce accurate maps of the bedrock depth for geotechnical analysis, then model adequacy is not as important as long as the simulated bedrock depths are in reasonable agreement with their point observations. High-fidelity and high-resolution bedrock depth maps can then be generated (with estimates of uncertainty) using a distributed parameterization of the DTB model. This does require the availability of a relatively dense network of borehole/geophysical observations and careful analysis of overfitting using split sampling and/or uncertainty analysis of the posterior maps sampled with DREAM. The simulation result of such distributed calibration approach was plotted in Figure 12 using a different gray color for the DTB parameter and model uncertainties. This posterior simulation of the bedrock depth can now be used for probabilistic geotechnical analysis to derive 95% uncertainty intervals of common metrics of slope stability and landslide potential. This framework embraces the conclusions of *Catani et al.* [2010], who used an infinite slope stability model with distributed bedrock depths and found that the soil thickness was probably the most significant "parameter" controlling the factor of safety. Indeed, one would expect the explicit treatment of bedrock depth uncertainty in geotechnical analysis to improve risk analysis and decision making.

In this paper, we have used a classical residual based likelihood function to quantify the agreement between the model and observational data. This statistical measure of model/data similarity is not rooted properly in geologic/geomorphic theory and has little correspondence to specific behaviors of the system. This makes it very difficult to detect model structural errors, our main intended goal in application of Bayesian methods. We therefore recommend the use of summary metrics of the calibration data instead. These statistics can be designed to measure theoretically relevant parts of system behavior, and diagnostic evaluation then proceeds with analysis of the behavioral (signature) similarities and differences between the system data and corresponding model simulation [*Gupta et al.*, 2008; *Vrugt and Sadegh*, 2013]. Ideally, these differences are then related to individual process descriptions, and model correction takes place by refining/improving these respective components of the model. Recent work has shown that such an approach provides better guidance on model malfunctioning and related issues than the conventional residual-based paradigm [*Sadegh et al.*, 2015]. The DREAM toolbox supports the use of summary statistics and diagnostic model evaluation [*Vrugt*, 2016].

The focus of our study has been only on a relatively small part of the PRB. A relatively large monetary investment would be required to obtain a high-quality bedrock depth data set for the entire watershed. This would also involve significant human commitment particularly on the steepest hillslopes of the PRB which are specifically difficult to access and dangerous to measure, even for well-trained professionals.

8. Summary and Conclusions

The depth to bedrock beneath soil-mantled landscapes controls a myriad of ecologic, hydrologic, geomorphologic, and atmospheric processes as it influences subsurface flow paths, erosion rates, soil moisture status, water uptake by plant roots, and latent and sensible heat fluxes. As hillslope interiors are very difficult to illuminate and access, the direct measurement of the bedrock depth is rather time consuming, and much effort and human commitment would be required to characterize adequately bedrock depth variations at spatial scales of a hillslope and watershed. Thus, a computer model that can simulate high-resolution spatial maps of the depth to bedrock is of great value and importance.

In this paper, we have introduced the different building blocks of a DTB model to predict the vertical extent of the weathered rock underling soil-mantled hillslopes from a high-resolution topographic map of the soil surface. Our model builds on the bottom-up control on fresh-bedrock hypothesis of *Rempe and Dietrich* [2014] and calculates the thickness of the weathered zone from the difference between the measured surface topography and predicted groundwater profile derived from analytic solution of the one-dimensional steady state Boussinesq equation. Two additional terms are used in our DTB model to characterize adequately the effect of mass movement on steep hillslopes, and the shape and depth of the bedrock surface in the drainage valley. Most of the model parameters can be measured directly in the laboratory or field using experiments on soil and rock mass samples, and simulated variables can be verified using cosmogenic nuclide measurements, geophysical imaging, topographic surveying, and drilling.

Bayesian analysis was used to reconcile the DTB-model predicted bedrock depths beneath hilltops, sideslopes, and valleys with field observations. This approach uses MCMC simulation with DREAM to search efficiently the model parameter space in pursuit of so-called posterior samples that best mimic the observed data. The quality of fit is measured by a likelihood function which summarizes in a single value the distance between the observed and simulated bedrock depths. The prior distribution summarizes all our knowledge about the model parameters before the field data are collected. This distribution should honor soft data, geologic observations, field expertise, and literature findings. Marginal distributions and pairs of bivariate scatter plots of the posterior samples generated with DREAM are used to assess parameter sensitivity and correlation. Predictive uncertainty can be assessed by evaluating the DTB model with each posterior parameter solution. The posterior mean bedrock depth map can then be compared to observed data to benchmark the performance of the DTB model and help verify structural weaknesses. This step is an integral part of the scientific method and key to model (hypothesis) refinement.

Two case studies with synthetic and real-world regolith depth data from the Papagaio river basin in Rio de Janeiro, Brazil were used to illustrate the usefulness and applicability of our DTB model and methodology. Our results demonstrate that the proposed DTB model with lumped parameters mimics reasonably well the observed regolith depth data with root mean square error (RMSE) of the posterior mean simulation of 1.52 m and 1.80 m for the synthetic and PRB evaluation data set, respectively. The performance of the DTB model can be enhanced if a distributed parameterization of Φ is used with RMSE for both data sets reduced to 1.47 and 1.76 m, respectively. The use of a distributed parameterization provides a means to account implicitly, and in a relatively simple way, for geologic/geomorphic watershed heterogeneities that are difficult, or impossible, to characterize adequately in the field.

The DTB simulated bedrock surface underneath the watershed can be used as input to hydromechanical models and should improve considerably the reliability of hillslope-scale simulations of shallow landslides and debris-flow. The posterior bedrock depth simulations of the DTB model also allow uncertainty quantification of some key output variables of hydromechanical models such as landslide potential and factor of safety. What is more, the availability of an accurate bedrock depth map also makes it easier to characterize adequately the impact of soil hydraulic and soil strength properties on slope stability.

References

Akaike, H. (1974), A new look at the statistical model identification, *IEEE Trans. Autom. Control*, 19(6), 716–723, doi:10.1109/TAC.1974.1100705.

Anderson, R. S., S. P. Anderson, and G. E. Tucker (2013), Rock damage and regolith transport by frost: An example of climate modulation of the geomorphology of the critical zone, *Earth Surf. Processes Landforms*, 38, 299–316, doi:10.1002/esp.3330.

Askarinejad, A., F. Casini, P. Bischof, A. Beck, and S. Springman (2012), Rainfall induced instabilities: A field experiment on a silty sand slope in northern Switzerland, *Riv. Ital. Geotecn.*, 3, 50–71.

Athapaththu, A. M. R. G., T. Tsuchida, and S. Kano (2014), A new geotechnical method for natural slope exploration and analysis, *Nat. Hazards*, 75(2), 1327–1348, doi:10.1007/s11069-014-1384-0.

Bear, J. (2013), *Dynamics of Fluids in Porous Media*, 784 pp., Dover, N. Y.

Bellugi, D., D. G. Milledge, W. E. Dietrich, J. A. McKean, J. T. Perron, E. B. Sudderth, and B. Kazian (2015), A spectral clustering search algorithm for predicting shallow landslide size and location, *J. Geophys. Res. Earth Surface*, 120, 300–324, doi:10.1002/2014JF003137.

Bertoldi, G., R. Rigon, and T. M. Over (2006), Impact of watershed geomorphic characteristics on the energy and water budgets, *J. Hydrometeorol.*, 7, 389–403, doi:10.1175/JHM500.1.

Boer, M., G. D. Barrio, and J. Puigdefábres (1996), Mapping soil depth classes in dry mediterranean areas using terrain attributes derived from a digital elevation model, *Geoderma*, 72(1-2), 99–118, doi:10.1016/0016-7061(96)00024-9.

Bohidar, R. N., J. P. Sullivan, and J. F. Hermance (2001), Delineating depth to bedrock beneath shallow unconfined aquifers: A gravity transect across the Palmer river basin, *Ground Water*, 39(5), 729–736, doi:10.1111/j.1745-6584.2001.tb02363.x.

Borja, R. I. and J. A. White (2010), Continuum deformation and stability analyses of a steep hillside slope under rainfall infiltration, *Acta Geotech.*, *5*(1), 1–14, doi:10.1007/s11440-009-0108-1.

Catani, F., S. Segoni, and G. Falorni (2010), An empirical geomorphology-based approach to the spatial prediction of soil thickness at catchment scale, *Water Resour. Res.*, *46*, W05508, doi:10.1029/2008WR007450.

Christensen, C. W., A. A. Pfaffhuber, H. Anschütz, and T. F. Smaavik (2015), Combining airborne electromagnetic and geotechnical data for automated depth to bedrock tracking, *J. Appl. Geophys.*, *119*, 178–191, doi:10.1016/j.jappgeo.2015.05.008.

Chung, J., and J. D. Rogers (2012), Estimating the position and variability of buried bedrock surfaces in the St. Louis metro area, *Eng. Geol.*, *126*, 37–45, doi:10.1016/j.enggeo.2011.12.007.

Clair J. St., S. Moon, W. S. Holbrook, J. T. Perron, C. S. Riebe, S. J. Martel, B. Carr, C. Harman, K. Singha, and D. deB. Richter (2015), Geophysical imaging reveals topographic stress control of bedrock weathering, *Science*, *350*(6260), 534–538, doi:10.1126/science.aab2210.

Dahlke, H. E., T. Behrens, J. Seibert, and L. Andersson (2009), Test of statistical means for the extrapolation of soil depth point information using overlays of spatial environmental data and bootstrapping techniques, *Hydrol. Processes*, *23*(21), 3017–3029, doi:10.1002/hyp.7413.

Davis, K., and Y. Li (2011), Fast solution of geophysical inversion using adaptive mesh, space-filling curves and wavelet compression, *Geophys. J. Int.*, *185*(1), 157–166, doi:10.1111/j.1365-246X.2011.04929.x.

DeRose, R. C., N. A. Trustrum, and P. M. Blaschke (1991), Geomorphic change implied by regolith-slope relationships on steepland hillslopes, Taranaki, New Zealand, *Catena*, *18*(5), 489–514, doi:10.1016/0341-8162(91)90051-X.

Dietrich, W. E., R. Reiss, M. -L. Hsu, and D. R. Montgomery (1995), A process-based model for colluvial soil depth and shallow landsliding using digital elevation data, *Hydrol. Processes*, *9*(3–4), 383–400, doi:10.1002/hyp.3360090311.

Ebel, B. A., K. Loague, W. E. Dietrich, D. R. Montgomery, R. Torres, S. P. Anderson, and T. W. Giambelluca (2007), Near-surface hydrologic response for a steep, unchanneled catchment near Coos Bay, Oregon: 1. Sprinkling experiments, *Am. J. Sci.*, *307*(4), 678–708, doi: 10.2475/04.2007.02.

Eguchi, S., M. Sawamoto, and M. Masahiko (2009), Field scale determination of the aquifer-aquitard boundary in Joso Clay by cone penetrometry, *Soil Sci. Plant Nutr.*, *55*(3), 337–348, doi:10.1111/j.1747-0765.2009.00377.x.

Feininger, T. (1971), Chemical weathering and glacial erosion of crystalline rocks and the origin of till, *U.S. Geol. Surv. Prof. Pap.*, *750-C*, C65–C81.

Fernandes, N. F., A. L. Coelho Netto, and W. A. Lacerda (1994), Subsurface hydrology of layered colluvium mantles in unchanneled valleys-south-Eastern Brazil, *Earth Surf. Processes Landforms*, *19*, 609–626, doi:10.1002/esp.3290190703.

Fernandes, N. F., R. F. Guimarães, R. A. Gomes, B. C. Vieira, D. R. Montgomery, and H. Greenberg (2004), Topographic controls of landslides in Rio de Janeiro: Field evidence and modeling, *Catena*, *55*(2), 163–181, doi:10.1016/S0341-8162(03)00115-2.

Freer, J., J. J. McDonnell, K. J., Beven, N. E., Peters, D. A. Burns, R. P. Hooper, B. Aulenbach, and C. Kendall (2002), The role of bedrock topography on subsurface storm flow, *Water Resour. Res.*, *38*(12), 1269, doi:10.1029/2001WR000872.

Fu, Z., Z. Li, C. Cai, Z. Shi, Q. Xu, and X. Wang (2011), Soil thickness effect on hydrological and erosion characteristics under sloping lands: A hydropedological perspective, *Geoderma*, *167–168*, 41–53, doi:10.1016/j.geoderma.2011.08.013.

Fujimoto, M., N. Ohte, and M. Tani (2008), Effects of hillslope topography on hydrological responses in a weathered granite mountain, Japan: Comparison of the runoff response between the valley-head and the side slope, *Hydrol. Processes*, *22*(14), 2581–2594, doi: 10.1002/hyp.6857.

Gelman, A., and D. B. Rubin (1992), Inference from iterative simulation using multiple sequences, *Stat. Sci.*, *7*(4), 457–472.

Gomes, R., R. Guimarães, O. de Carvalho Jr., N. Fernandes, E. Vargas Jr., and E. Martins (2008), Identification of the affected areas by mass movement through a physically based model of landslide hazard combined with an empirical model of debris flow, *Nat. Hazards*, *45*(2), 197–209, doi:10.1007/s11069-007-9160-z.

Gomes, R., R. Guimarães, O. de Carvalho Jr., N. Fernandes, and E. Vargas Jr. (2013), Combining spatial models for shallow landslides and debris-flows prediction, *Remote Sens.*, *5*(5), 2219–2237, doi:10.3390/rs5052219.

Goovaerts, P. (1997), *Geostatistics for Natural Resources Evaluation*, 1st ed., 496 pp., Oxford Univ. Press, N. Y.

Guimarães, R., D. R. Montgomery, H. M. Greenberg, N. Fernandes, R. Gomes, and O. de Carvalho Jr. (2003), Parameterization of soil properties for a model of topographic controls on shallow landsliding: Application to Rio de Janeiro, *Eng. Geol.*, *69*(1-2), 99–108, doi:10.1016/S0013-7952(02)00263-6.

Gupta, H. V., T. Wagener, and Y. Liu (2008), Reconciling theory with observations: Elements of a diagnostic approach to model evaluation, *Hydrol. Processes*, *22*(18), 3802–3813, doi:10.1002/hyp.6989.

He, M., T. S. Hogue, K. J. Franz, S. A. Margulis, and J. A. Vrugt (2011), Characterizing parameter sensitivity and uncertainty for a snow model across hydroclimatic regimes, *Adv. Water Resour.*, *34*(1), 114–127, doi:10.1016/j.advwatres.2010.10.002.

Heimsath, A. M., W. E. Dietrich, K. Nishiizumi, and R. C. Finkel (2001), Stochastic processes of soil production and transport: Erosion rates, topographic variation and cosmogenic nuclides in the Oregon Coast Range, *Earth Surf. Processes Landforms*, *26*(5), 531–552, doi: 10.1002/esp.209.

Ho, J.-Y., K. T. Lee, T. -C. Chang, Z. -Y. Wang, and Y. -H. Liao (2012), Influences of spatial distribution of soil thickness on shallow landslide prediction, *Eng. Geol.*, *124*, 38–46, doi:10.1016/j.enggeo.2011.09.013.

Hopp, L., and J. McDonnell (2009), Connectivity at the hillslope scale: Identifying interactions between storm size, bedrock permeability, slope angle and soil depth, *J. Hydrol.*, *376*(3–4), 378–391, doi:10.1016/j.jhydrol.2009.07.047.

Hurst, M. D., S. M. Mudd, R. Walcott, M. Attal, and K. Yoo (2012), Using hilltop curvature to derive the spatial distribution of erosion rates, *J. Geophys. Res.*, *117*, F02017, doi:10.1029/2011JF002057.

Jafarpour, B. (2011), Wavelet reconstruction of geologic facies from nonlinear dynamic flow measurements, *IEEE Trans. Geosci. Remote Sens.*, *49*(5), 1520–1535, doi:10.1109/TGRS.2010.2089464.

Jenny, H. (1941), *Factors of Soil Formation: A Quantitative System in Pedology*, 281 pp., McGraw-Hill, N. Y.

Keating, E. H., J. Doherty, J. A. Vrugt, and Q. Kang (2010), Optimization and uncertainty assessment of strongly nonlinear groundwater models with high parameter dimensionality, *Water Resour. Res.*, *46*, W10517, doi:10.1029/2009WR008584.

Kim, M. S., Y. Onda, J. K. Kim, and S. W. Kim (2015), Effect of topography and soil parameterisation representing soil thicknesses on shallow landslide modelling, *Quat. Int.*, *384*, 91–106, doi:10.1016/j.quaint.2015.03.057.

Kosugi, K., S. Katsura, M. Katsuyama, and T. Mizuyama (2006), Water flow processes in weathered granitic bedrock and their effects on runoff generation in a small headwater catchment, *Water Resour. Res.*, *42*, W02414, doi:10.1029/2005WR004275.

Kosugi, K., Y. Yamakawa, N. Masaoka, and T. Mizuyama (2009), A combined penetrometer-moisture probe for surveying soil properties of natural hillslopes, *Vadose Zone J.*, *8*(1), 52–63, doi:10.2136/vzj2008.0033.

Kuriakose, S. L., S. Devkota, D. Rossiter, and V. Jetten (2009), Prediction of soil depth using environmental variables in an anthropogenic landscape, a case study in the Western Ghats of Kerala, India, *Catena*, *79*(1), 27–38, doi:10.1016/j.catena.2009.05.005.

Laloy, E., N. Linde, and J. A. Vrugt (2012), Mass conservative three-dimensional water tracer distribution from Markov chain Monte Carlo inversion of time-lapse ground-penetrating radar data, *Water Resour. Res.*, *48*, W07510, doi:10.1029/2011WR011238.

Laloy, E., B. Rogiers, J. A. Vrugt, D. Mallants, and D. Jacques (2013), Efficient posterior exploration of a high-dimensional groundwater model from two-stage Markov chain Monte Carlo simulation and polynomial chaos expansion, *Water Resour. Res.*, *49*, 2664–2682, doi:10.1002/wrcr.20226.

Lanni, C., M. Borga, R. Rigon, and P. Tarolli (2012), Modelling shallow landslide susceptibility by means of a subsurface flow path connectivity index and estimates of soil depth spatial distribution, *Hydrol. Earth Syst. Sci.*, *16*(11), 3959–3971, doi:10.5194/hess-16-3959-2012.

Lanni, C., J. McDonnell, L. Hopp, and R. Rigon (2013), Simulated effect of soil depth and bedrock topography on near-surface hydrologic response and slope stability, *Earth Surf. Processes Landforms*, *38*(2), 146–159, doi:10.1002/esp.3267.

Lebedeva, M. I., and S. L. Brantley (2013), Exploring geochemical controls on weathering and erosion of convex hillslopes: Beyond the empirical regolith production function, *Earth Surf. Processes Landforms*, *38*, 1793–1807, doi:10.1002/esp.3424.

Liang, W. -L., and T. Uchida (2014), Effects of topography and soil depth on saturated-zone dynamics in steep hillslopes explored using the three-dimensional Richards' equation, *J. Hydrol.*, *510*, 124–136, doi:10.1016/j.jhydrol.2013.12.029.

Linde, N., and J. A. Vrugt (2013), Distributed soil moisture from crosshole ground-penetrating radar travel times using stochastic inversion, *Vadose Zone J.*, *12*(1), doi:10.2136/vzj2012.0101.

Liu, J., X. Chen, H. Lin, H. Liu, and H. Song (2013), A simple geomorphic-based analytical model for predicting the spatial distribution of soil thickness in headwater hillslopes and catchments, *Water Resour. Res.*, *49*, 7733–7746, doi:10.1002/2013WR013834.

Lochbühler, T., S. J. Breen, R. L. Detwiler, J. A. Vrugt, and N. Linde (2014), Probabilistic electrical resistivity tomography of a CO_2 sequestration analog, *J. Appl. Geophys.*, *107*, 80–92, doi:10.1016/j.jappgeo.2014.05.013.

Lochbühler, T., J. A. Vrugt, M. Sadegh, and N. Linde (2015), Summary statistics from training images as prior information in probabilistic inversion, *Geophys. J. Int.*, *201*(1), 157–171, doi:10.1093/gji/ggv008.

Lucà, F., G. Buttafuoco, G. Robustelli, and A. Malafronte (2014), Spatial modelling and uncertainty assessment of pyroclastic cover thickness in the Sorrento Peninsula, *Environ. Earth Sci.*, *72*(9), 3353–3367, doi:10.1007/s12665-014-3241-6.

Masaoka, N., K. Kosugi, Y. Yamakawa, T. Mizuyama, and D. Tsutsumi (2012), Application of a combined Penetrometer-moisture probe for investigating heterogeneous hydrological properties of a footslope area, *Vadose Zone J.*, *11*(2), doi:10.2136/vzj2011.0064.

Metropolis, N., A. W. Rosenbluth, M. N. Rosenbluth, A. H. Teller, and E. Teller (1953), Equation of state calculations by fast computing machines, *J. Chem. Phys.*, *21*(6), 1087–1092, doi:10.1063/1.1699114.

Mey, J., D. Scherler, G. Zeilinger, and M. R. Strecker (2015), Estimating the fill thickness and bedrock topography in intermontane valleys using artificial neural networks, *J. Geophys. Res. Earth Surface*, *120*, 1301–1320, doi:10.1002/2014JF003270.

Milledge, D. G., D. Bellugi, J. A. McKean, A. L. Densmore, and W. E. Dietrich (2014), A multidimensional stability model for predicting shallow landslide size and shape across landscapes, *J. Geophys. Res. Earth Surface*, *119*, 2481–2504, doi:10.1002/2014JF003135.

Mukhlisin, M., M. Taha, and K. Kosugi (2008), Numerical analysis of effective soil porosity and soil thickness effects on slope stability at a hillslope of weathered granitic soil formation, *Geosci. J.*, *12*(4), 401–410, doi:10.1007/s12303-008-0039-0.

Odeh, I. O. A., D. J. Chittleborough, and A. B. McBratney (1991), Elucidation of soil-landform interrelationships by canonical ordination analysis, *Geoderma*, *49*(1-2), 1–32, doi:10.1016/0016-7061(91)90089-C.

Odeh, I. O. A., A. B. McBratney, and D. J. Chittleborough (1995), Further results on prediction of soil properties from terrain attributes: Heterotopic cokriging and regression-kriging, *Geoderma*, *67*(3-4), 215–226, doi:10.1016/0016-7061(95)00007-B.

Ohnuki, Y., C. Kimhean, Y. Shinomiya, and J. Toriyama (2008), Distribution and characteristics of soil thickness and effects upon water storage in forested areas of Cambodia, *Hydrol. Processes*, *22*(9), 1272–1280, doi:10.1002/hyp.6937.

Oware, E. K., S. M. J. Moysey, and T. Khan (2013), Physically based regularization of hydrogeophysical inverse problems for improved imaging of process-driven systems, *Water Resour. Res.*, *49*, 6238–6247, doi:10.1002/wrcr.20462.

Pelletier, J. D., and C. Rasmussen (2009), Geomorphically based predictive mapping of soil thickness in upland watersheds, *Water Resour. Res.*, *45*, W09417, doi:10.1029/2008WR007319.

Pelletier, J. D., et al. (2011), Calibration and testing of upland hillslope evolution models in a dated landscape: Banco Bonito, New Mexico, *J. Geophys. Res.*, *116*, F04004, doi:10.1029/2011JF001976.

Perron, J. T. (2011), Numerical methods for nonlinear hillslope transport laws, *J. Geophys. Res.*, *116*, F02021, doi:10.1029/2010JF001801.

Rempe, D. M., and W. E. Dietrich (2014), A bottom-up control on fresh-bedrock topography under landscapes, *Proc. Natl. Acad. Sci. U. S. A.*, *111*(18), 6576–6581, doi:10.1073/pnas.1404763111.

Reu, J. D., et al. (2013), Application of the topographic position index to heterogeneous landscapes, *Geomorphology*, *186*, 39–49, doi:10.1016/j.geomorph.2012.12.015.

Roering, J. J. (2008), How well can hillslope evolution models" explain" topography? Simulating soil transport and production with high-resolution topographic data, *Geol. Soc. Am. Bull.*, *120*(9-10), 1248–1262, doi:10.1130/B26283.1.

Roering, J. J., J. W. Kirchner, and W. E. Dietrich (1999), Evidence for nonlinear, diffusive sediment transport on hillslopes and implications for landscape morphology, *Water Resour. Res.*, *35*(3), 853–870, doi:10.1029/1998WR900090.

Roering, J.J., J. A. Marshall, A. Booth, M. Mort, and Q. Jin, (2010), Evidence for biotic controls on topography and soil production, *Earth Planet. Sci. Lett.*, *298*, 183–190, doi:10.1016/j.epsl.2010.07.040.

Ruddock, E. C. (1967) Residual soils of the Kumasi district in Ghana, *Géotechnique*, *17*(4), 359–377, doi:10.1680/geot.1967.17.4.359.

Ruxton B. P., and L. Berry (1959), The basal rock surface on weathered granitic rocks, *Proc. Geol. Assoc.*, *70*(4), 290–295, doi:10.1016/S0016-7878(59)80010-9.

Saco, P. M., G. R. Willgoose, and G. R. Hancock (2006), Spatial organization of soil depths using a landform evolution model, *J. Geophys. Res.*, *111*, F02016, doi:10.1029/2005JF000351.

Sadegh M., J. A. Vrugt, C. Xu, and E. Volpi (2015), The stationarity paradigm revisited: Hypothesis testing using diagnostics, summary metrics, and DREAM$_{(ABC)}$, *Water Resour. Res.*, *51*, 9207–9231, doi:10.1002/2014WR016805.

Sarkar, S. A., K. Roy, and T. R. Martha (2013), Soil depth estimation through soil-landscape modelling using regression kriging in a Himalayan terrain, *Int. J. Geogr. Inform. Sci.*, *27*(12), 2436–2454, doi:10.1080/13658816.2013.814780.

Saulnier, G.-M., K. Beven, and C. Obled (1997), Including spatially variable effective soil depths in TOPMODEL, *J. Hydrol.*, *202*(1–4), 158–172, doi:10.1016/S0022-1694(97)00059-0.

Scharnagl, B., J. A. Vrugt, H. Vereecken, and M. Herbst (2011), Inverse modelling of in situ soil water dynamics: Investigating the effect of different prior distributions of the soil hydraulic parameters, *Hydrol. Earth Syst. Sci.*, *15*(10), 3043–3059, doi:10.5194/hess-15-3043-2011.

Shafique, M., M. van der Meijde, and S. Ullah (2011), Regolith modeling and its relation to earthquake induced building damage: A remote sensing approach, *J. Asian Earth Sci.*, *42*(1-2), 65–75, doi:10.1016/j.jseaes.2011.04.004.

Sitharam, T., P. Samui, and P. Anbazhagan (2008) Spatial variability of rock depth in Bangalore using geostatistical, neural network and support vector machine models, *Geotech. Geol. Eng.*, *26*(5), 503–517, doi:10.1007/s10706-008-9185-4.

Stewart, M. T. (1980), Gravity survey of a deep buried valley, *Ground Water*, *18*, 24–30, doi:10.1111/j.1745-6584.1980.tb03367.x.

Tarolli, P., and G. D. Fontana (2009), Hillslope-to-valley transition morphology: New opportunities from high resolution DTMs, *Geomorphology*, *113*(1-2), 47–56, doi:10.1016/j.geomorph.

Tesfa, T. K., D. G. Tarboton, D. G. Chandler, and J. P. McNamara (2009), Modeling soil depth from topographic and land cover attributes, *Water Resour. Res.*, *45*, W10438, doi:10.1029/2008WR007474.

Thomas, M. F. (1966), Implications of deep weathering patterns in crystalline rocks in Nigeria, *Trans. Inst. Brit. Geogr.*, *40*, 173–193, doi: 10.2307/621576.

Troch, P.A., E. van Loon, and A. Hilberts (2002), Analytical solutions to a hillslope-storage kinematic wave equations for subsurface flow, *Adv. Water Resour.*, *25*, 637–649, doi:10.1016/S0309-1708(02)00017-9.

Tromp-van Meerveld, H. J., and J. J. McDonnell (2006a), Threshold relations in subsurface stormflow: 1. A 147-storm analysis of the Panola hillslope, *Water Resour. Res*, *42*, W02410, doi:10.1029/2004WR003778.

Tromp-van Meerveld, H. J., and J. J. McDonnell (2006b), Threshold relations in subsurface stormflow: 2. The fill and spill hypothesis, *Water Resour. Res.*, *42*, W02411, doi:10.1029/2004WR003800.

Tsuchida T., A. M. R. G. Athapaththu, S. Kano, and K. Suga (2011), Estimation of in situ shear strength parameters of weathered granitic (Masado) slopes using lightweight dynamic cone penetrometer, *Soils Found.*, *51*(3), 497–512.

Tye, A. M., R. L. Lawley, M. A. Ellis, and B. G. Rawlins (2011), The spatial variation of weathering and soil depth across a Triassic sandstone outcrop, *Earth Surf. Processes Landforms*, *36*(5), 569–581, doi:10.1002/esp.2075.

Vargas Jr. E. A., R. C. Velloso, T. M. P. de Campos, and L. M. Costa Filho (1990), Saturated-unsaturated analysis of water flow in slopes of Rio de Janeiro, Brazil, *Comput. Geotech.*, *10*(3), 247–261, doi:10.1016/0266-352X(90)90038-W.

Vieira, B. C., and N. F. Fernandes (2004), Landslides in Rio de Janeiro: The role played by variations in soil hydraulic conductivity, *Hydrol. Processes*, *18*(4), 791–805, doi:10.1002/hyp.1363.

Vrugt, J. A. (2016), Markov chain Monte Carlo simulation using the DREAM software package: Theory, concepts, and MATLAB Implementation, *Environ. Modell. Software*, *75*, 273–316, doi:10.1016/j.envsoft.2015.08.013.

Vrugt, J. A., and M. Sadegh (2013), Toward diagnostic model calibration and evaluation: Approximate Bayesian computation, *Water Resour. Res.*, *49*, 4335–4345, doi:10.1002/wrcr.20354.

Vrugt, J. A., C. J. F. ter Braak, M. P. Clark, J. M. Hyman, and B. A. Robinson (2008), Treatment of input uncertainty in hydrologic modeling: Doing hydrology backward with Markov chain Monte Carlo simulation, *Water Resour. Res.*, *44*, W00B09, doi:10.1029/2007WR006720.

Vrugt, J. A., C. J. F. ter Braak, C. G. H. Diks, B. A. Robinson, J. M. Hyman, and D. Higdon (2009) Accelerating Markov chain Monte Carlo simulation by differential evolution with self-adaptive randomized subspace sampling, *Int. J. Nonl. Sci. Numer. Simul.*, *10*(3), 273–290, doi: 10.1002/esp.3423.

Yang, Q., F. Zhang, Z. Jiang, W. Li, J. Zhang, F. Zeng, and H. Li (2014) Relationship between soil depth and terrain attributes in karst region in Southwest China, *J. Soils Sediment.*, *14*(9), 1568–1576, doi:10.1007/s11368-014-0904-6.

Wiegand, C., K. Kringer, C. Geitner, and M. Rutzinger (2013), Regolith structure analysis: A contribution to understanding the local occurrence of shallow landslides (Austrian Tyrol), *Geomorphology*, *180*(3), 5–13, doi:10.1016/j.geomorph.2012.06.027.

Wilford, J., and M. Thomas (2013), Predicting regolith thickness in the complex weathering setting of the central Mt Lofty Ranges, South Australia, *Geoderma*, *206*, 1–13, doi:10.1016/j.geoderma.2013.04.002.

Zhou, Y., and X. Wu (1994), Use of neural networks in the analysis and interpretation of site investigation data, *Comput. Geotech.*, *16*(2), 105–122, doi:10.1016/0266-352X(94)90017-5.

Zhou, W., B. F. Beck, and J. B. Stephenson (2000), Reliability of dipole-dipole electrical resistivity tomography for defining depth to bedrock in covered karst terranes, *Environ. Geol.*, *39*(7), 760–766, doi:10.1007/s002540050491.

Ziadat, F. (2005), Analyzing digital terrain attributes to predict soil attributes for a relatively large area, *Soil Sci. Soc. Am. J.*, *69*(5), 1590–1599, doi:10.2136/sssaj2003.0264.

Ziadat, F. (2010), Prediction of soil depth from digital terrain data by integrating statistical and visual approaches, *Pedosphere*, *20*(3), 361–367, doi:10.1016/S1002-0160(10)60025-2.